

Influences of tropical–extratropical interaction on the multidecadal AMOC variability in the NCEP climate forecast system

Bohua Huang · Zeng-Zhen Hu · Edwin K. Schneider · Zhaohua Wu · Yan Xue · Barry Klinger

Received: 21 March 2011 / Accepted: 23 November 2011
© Springer-Verlag 2011

Abstract We have examined the mechanisms of a multidecadal oscillation of the Atlantic Meridional Overturning Circulation (AMOC) in a 335-year simulation of the Climate Forecast System (CFS), the climate prediction model developed at the National Centers for Environmental Prediction (NCEP). Both the mean and seasonal cycle of the AMOC in the CFS are generally consistent with observation-based estimates with a maximum northward volume transport of 16 Sv ($10^6 \text{ m}^3/\text{s}$) near 35°N at 1.2 km. The annual mean AMOC shows an intermittent quasi 30-year oscillation. Its dominant structure includes a deep anomalous overturning cell (referred to as the anomalous AMOC) with amplitude of 0.6 Sv near 35°N and an anomalous subtropical cell (STC) of shallow overturning spanning across the equator. The mechanism for the oscillation includes a positive feedback between the

anomalous AMOC and surface wind stress anomalies in mid-latitudes and a negative feedback between the anomalous STC and AMOC. A strong AMOC is associated with warm sea surface temperature anomaly (SSTA) centered near 45°N , which generates an anticyclonic easterly surface wind anomaly. This anticyclonic wind anomaly enhances the regional downwelling and reinforces the anomalous AMOC. In the mean time, a wind-evaporation-SST (WES) feedback extends the warm SSTA to the tropics and induces a cyclonic wind stress anomaly there, which drives a tropical upwelling and weakens the STC north of the equator. The STC anomaly, in turn, drives a cold upper ocean heat content anomaly (HCA) in the northern tropical Atlantic and weakens the meridional heat transport from the tropics to the mid-latitude through an anomalous southward western boundary current. The anomalous STC transports cold HCA from the subtropics to the mid-latitudes, weakening the mid-latitude deep overturning.

B. Huang · E. K. Schneider · B. Klinger
Department of Atmospheric, Oceanic, and Earth Sciences,
College of Science, Gorge Mason University,
4400 University Drive, Fairfax, VA 22030, USA

B. Huang (✉) · E. K. Schneider · B. Klinger
Center for Ocean-Land-Atmosphere Studies, Institute of Global
Environment and Society, 4041 Powder Mill Road,
#302, Calverton, MD 20705, USA
e-mail: huangb@cola.iges.org

Z.-Z. Hu · Y. Xue
Climate Prediction Center, National Centers for Environmental
Prediction/NOAA, 5200 Auth Road, Camp Springs,
MD 20746, USA

Z. Wu
Department of Earth, Ocean, and Atmospheric Science,
Center for Ocean-Atmospheric Prediction Studies, Florida State
University, 1017 Academic Way, Tallahassee, FL 32306, USA

1 Introduction

Sea surface temperature (SST) observations since the late nineteenth century reveal an apparent “Atlantic Multidecadal Oscillation” (AMO, Kerr 2000) dominated by anomalies of the same sign across the North Atlantic. Peak values form a horseshoe-shaped pattern spanning the Atlantic at $40\text{--}50^\circ\text{N}$, extending southward near Africa, and continuing westward near 20°N (Folland et al. 1986; Kushnir 1994; Enfield et al. 2001; Sutton and Hodson 2007, among others). Though sampling and instrumental problems contribute to observational uncertainty, the AMO (sometimes referred to as Atlantic Multidecadal Variability) is corroborated by much longer time series of proxy data (Gray et al. 2004; Delworth and Mann 2000).

Previous studies (e.g., Knight et al. 2005; Latif et al. 2006; Semenov et al. 2010, among others) have suggested that the AMO is the surface manifestation of fluctuations of the Atlantic Meridional Overturning Circulation (AMOC). The AMOC consists of net northward flow in the upper 1 km and southward return flow from about 1 to 4 km, linked by sinking north of 60°N and diffuse upwelling primarily in the Southern Ocean and Indo-Pacific basins. The AMOC's northward heat transport plays a crucial role in the global heat balance (Ganachaud and Wunsch 2000) and the climate in North America and Europe. Experiments with ocean–atmosphere coupled general circulation models (CGCMs) show that a large increase in surface freshwater flux in the AMOC sinking region (e.g., Manabe and Stouffer 1988; Timmermann et al. 2005; Dahl et al. 2005; Stouffer et al. 2006; Hu et al. 2008) substantially slows the AMOC within 10 years (Vellinga and Wood 2002). The reduction of heat transport cools down the North Atlantic SST in a pattern broadly resembling the AMO cold phase (e.g., Dong and Sutton 2002). Some CGCM simulations in Phase 3 of the Coupled Model Intercomparison Project (CMIP3) show a robust horseshoe-shaped SST pattern on multidecadal scales that are arguably related to the AMOC fluctuations (Ting et al. 2010). However, Wen et al. (2010) suggest that a drop in the AMOC transport by 6 Sv, which seems beyond the natural range, is needed to cause significant SST anomalies in the tropical Atlantic. Whether the natural AMOC fluctuation accounts for the observed AMO needs further evidence.

To understand the influence of the multidecadal AMOC variability on the SST, we should first understand the mechanisms of the multidecadal AMOC variability. Although many CGCMs can produce such fluctuations (e.g., Delworth et al. 1993; Timmermann et al. 1998; Cheng et al. 2004; Dong and Sutton 2005; Danabasoglu 2008), their causes seem diverse, as reflected by the wide range of oscillatory periods from 20 (e.g., Danabasoglu 2008) to 70–80 years (e.g., Jungclaus et al. 2005) and longer (Vellinga and Wu 2004). An underlying cause seems to be the time lag between temperature and salinity anomalies in the formation area of the North Atlantic Deep Water because the AMOC-induced temperature anomalies drive an anomalous gyre circulation, which subsequently advects salinity anomalies (Delworth et al. 1993). Some idealized ocean-only models can also show this kind of behavior (e.g., Weaver and Sarachik 1991). The physics determining the time scale of this oscillation, however, has yet to be pinned down (Delworth et al. 2007). On the other hand, the westward propagation of mid-latitude temperature anomalies alone may also cause AMOC fluctuations (Huck et al. 1999; Te Raa and Dijkstra 2002; Zhu and Jungclaus 2008; Park and Hwang 2009). These two mechanisms are consistent with the two major bands of

frequencies found at round 20–30 and 50–80 years in observations and models (Frankcombe et al. 2010). The former is associated with temperature propagation while the latter is more strongly affected by salinity. To further understand the characteristics of these different mechanisms, it is helpful to examine these processes separately in the CGCM context.

Although functioning in CGCMs, these mechanisms have been construed as either unstable modes (Huck et al. 2001) or damped oceanic oscillations (Delworth and Greatbatch 2000) in idealized uncoupled ocean model experiments. Whether air–sea feedback plays any role in forming or sustaining these oscillations is still an unsolved question. On the other hand, many CGCM studies mentioned above displayed a close link between the multidecadal variations of the AMOC and the North Atlantic Oscillation (NAO, e.g., Delworth et al. 1993; Dong and Sutton 2005; Danabasoglu 2008). However, it is unclear whether the low-frequency NAO is a passive response to the AMOC-induced SST anomalies, a random atmospheric forcing, or an indication of air–sea coupling. Delworth and Greatbatch (2000) argue that the NAO fluctuations simply stimulate the ocean internal mode through surface heat flux anomalies. Examining the water-hosing experiments, Chiang and Bitz (2005), Dahl et al. (2005), and Broccoli et al. (2006), among others, showed that the SST cooling in high latitudes is transmitted to the subtropics because of the thermodynamic feedbacks between the surface wind, evaporation and SST (WES, Chang et al. 1997; Xie 1999), which generates surface wind and SST anomalies resembling the NAO and AMO patterns. Examining the multidecadal oscillation in a CGCM, Timmermann et al. (1998) found that the AMOC-induced NAO change modulates the evaporation in the North Atlantic and the freshwater exchange with the Greenland Sea. Weaver and Valcke (1998) also argued that the multidecadal AMOC variability is a coupled mode.

The search for the coupled mechanisms is currently concentrated on the surface buoyancy effects but little is known about the influences of the surface wind stress over the North Atlantic. It can be argued that the dynamical forcing of the AMOC-induced wind stress anomalies may play a more significant role in the AMOC variability than the papers cited above indicate. Marshall et al. (2001) proposed an idealized model in which anomalous wind curl drives an anomalous gyre straddling the subtropical and subpolar gyres and the heat transport of this ‘intergyre’ gyre causes a delayed response to the mid-latitude wind stress on decadal time scales. The earlier study by Weng and Neelin (1998) also discussed a similar mechanism. Correspondingly, Alvarez-Garcia et al. (2008) demonstrated that these wind anomalies generate shallow overturning subtropical circulation (STC) anomalies on decadal time scales in an ocean model. Häkkinen and Rhines

(2009) found that a northeastward tilt of the zero line in the wind stress curl field since 2000 expanded the subtropical gyre and increased the penetration of the subtropical waters toward the Nordic Seas. It weakened the subpolar gyre simultaneously. Eden and Willebrand (2000) found that Ekman transport from observed winds may drive multi-decadal North Atlantic deep overturning anomalies, while Böning et al. (2006) also found complex links between the wind-driven subpolar flow and the meridional overturning. CGCM studies have not discussed oscillations resulting from interaction between the wind stress and the ocean overturning.

In this paper, we examine a CGCM multidecadal Atlantic oscillation in which feedback between AMOC and wind stress anomalies play a key role in amplifying both. We also find important interactions between the subtropical variability in the upper ocean and the AMOC fluctuations associated with the mid-latitude temperature anomalies. We concentrate on (1) how effectively WES can propagate the AMOC-induced SST and wind anomalies in mid and high latitudes into the subtropics and (2) whether the resultant anomalous subtropical winds lead to a significant feedback to the higher latitudes. The paper is structured as follows: Sect. 2 describes the CGCM and the experimental design. The multidecadal variability of the AMOC is identified in Sect. 3, a typical oscillation lifecycle is examined in Sect. 4, and physical mechanisms responsible for atmosphere–ocean feedback are examined in Sect. 5. The summary and conclusion are given in Sect. 6.

2 The CGCM simulation

The CGCM used in this study is the Climate Forecast System (CFS) developed at the National Centers for Environmental Prediction (NCEP) and has been the operational climate forecast model there from 2004 to 2011 (Saha et al. 2006). The atmosphere has a spectral expansion of spherical harmonics at a triangular truncation at T62 (~ 210 km grid spacing) and 64 vertical (σ -coordinate) levels. The greenhouse gas concentrations are held fixed at present-day level.

The oceanic component is the global (non-polar) Geophysical Fluid Dynamics Laboratory (GFDL) Modular Ocean Model (MOM Version 3, Pacanowski and Griffies 1998), extending from 74°S to 64°N . The model horizontal grid is $1^{\circ} \times 1^{\circ}$ poleward of 30°S and 30°N with the meridional resolution increasing gradually to $1/3^{\circ}$ between 10°S and 10°N . Vertically, it has 40 z -coordinate levels, with 27 in the upper 400 m. The subgrid mixing parameterization includes the non-local K-profile vertical turbulent mixing in the planetary boundary layer (Large et al. 1994) and quasi-isopycnal tracer mixing by mesoscale

eddies (Gent and McWilliams 1990). The model temperature and salinity are relaxed toward observed climatology of monthly temperature and salinity in the sponge layers near the model northern and southern boundaries. The oceanic and atmospheric components are coupled once per simulated day without flux correction. Our simulation was initialized from the observed ocean-atmospheric state on January 1, 1985, which is derived from the NCEP Reanalysis II (Kanamitsu et al. 2002) for the atmospheric state and the NCEP Global Ocean Data Assimilation System (GODAS, Behringer and Xue 2004) for the oceanic state. The integration has been conducted for 385 years. For this analysis, we have discarded the first 50 years as spin-up and used the last 335 years.

Compared with other climate models, a potential limitation of the AMOC simulation by the CFS is the non-polar configuration and the lack of sea ice in its oceanic component. However, it turns out that the simulated mean AMOC transport is generally realistic outside the sponge layer near the model northern boundary at 65°N . The mean meridional overturning stream function within the Atlantic Ocean averaged over the 335-year simulation demonstrates two deep overturning circulation cells throughout the basin (Fig. 1a). The upper cell depicts a clockwise circulation in the upper 3 km associated with sinking in the higher northern latitudes between 50°N and 60°N . Its maximum northward transport is shown by the positive centers of the stream function and to be referred to as the positive cell, as well as the AMOC, hereafter. The warm waters flow northward to replace the cold deep southward flow, with a maximum exchange of 16 Sv (10^6 m³/s) between 30°N and 45°N . Superimposed on the AMOC are the shallow subtropical cells (STCs) within the upper few hundreds of meters that are anti-symmetric with respect to the equator (Schott et al. 2004). The AMOC pattern and strength, as well as the STC, are qualitatively comparable to those produced by the 26-year GODAS ocean analysis (Fig. 1b), calculated from the same ocean model in uncoupled mode under the forcing of the surface fluxes from the NCEP reanalysis II while assimilating the observed temperatures from 1979 to 2004 into the upper 700 m of the ocean (Behringer and Xue 2004). The AMOC transport in the GODAS is also 16 Sv at its peak near 40°N though it is generally weaker than that of CFS in the subtropics (Fig. 1c). The AMOC strengths from both the CFS simulation and the GODAS analysis are qualitatively consistent with other model and observation-based estimates although they are on the lower side of the observational estimates of 16–18 Sv from zonal hydrographic sections (e.g., Ganachaud and Wunsch 2000; Talley et al. 2003; Lumpkin and Speer 2003, 2007). The most recent estimate based on the RAPID-MOCHA trans-basin observing array installed along 26.5°N puts the value at 18.5 Sv (Johns et al. 2011), which seems to be close to the

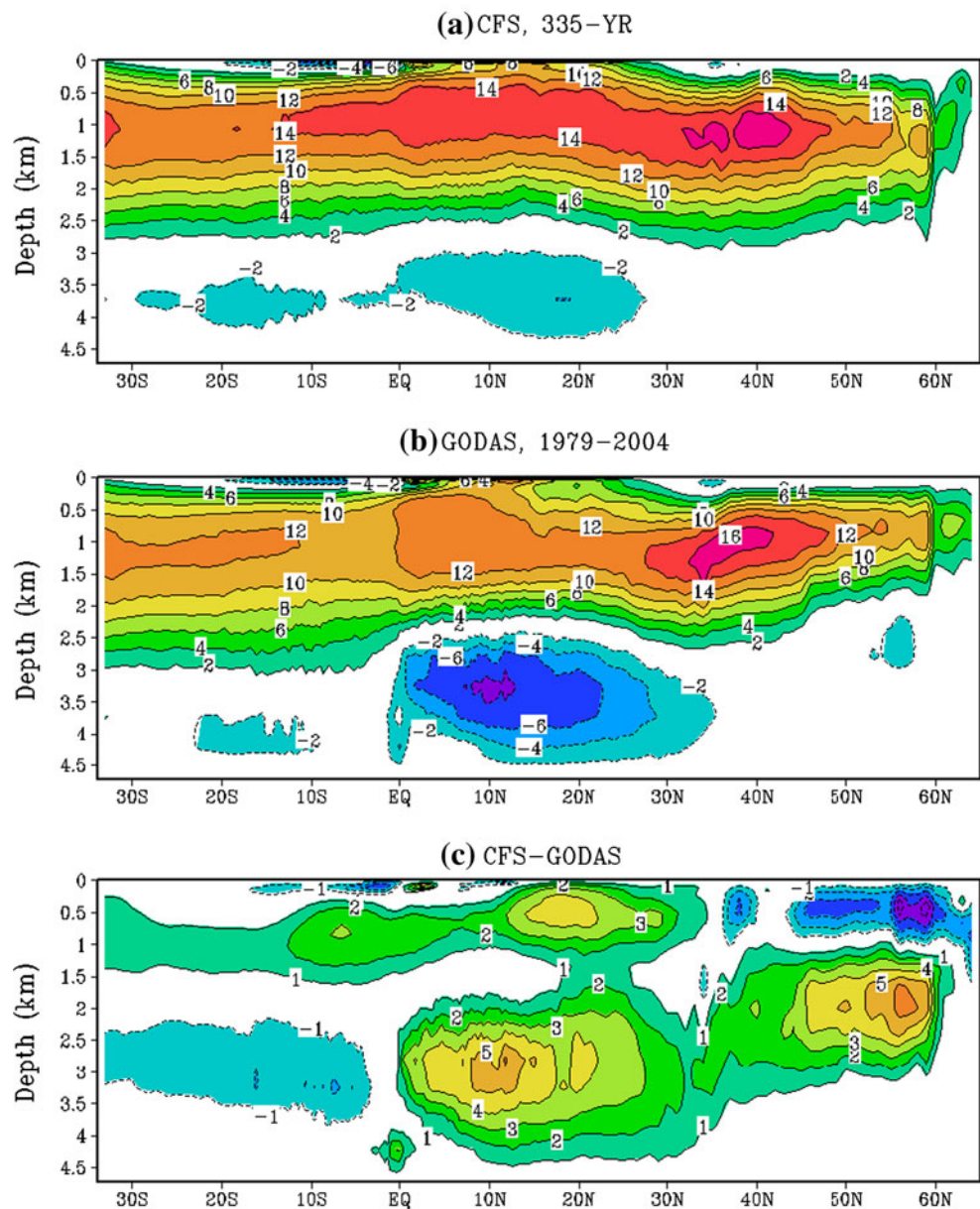
AMOC strength estimated from the European Centre for Medium Range Weather Forecasts' operational ocean analysis for the period 1959–2006 (Balmaseda et al. 2007). In addition, there is a clear anticlockwise (negative) bottom cell in both the CFS and GODAS, which is fed by the Antarctic Bottom Water and occupies the lower portion of the Atlantic basin. The strength of this cell is 2 Sv in CFS, significantly weaker than 8 Sv in GODAS (Fig. 1b). Compared with the observational estimate of 6 Sv by Talley et al. (2003), the CFS (GODAS) underestimates (overestimates) the intensity of this bottom cell.

Figure 2 shows the seasonal departures of the CFS monthly AMOC climatology from its long-term mean. The

December–February (DJF) seasonal departure (Fig. 2a) is characterized by an intensive anomalous positive cell in full depth within 20°S–30°N with the negative cells poleward on both sides. A similar pattern with opposite signs appears in June–August (JJA), featuring a negative tropical cell (Fig. 2c). Compared with the strong positive tropical departure in DJF, the negative tropical departure is weaker in its peak but stays longer from March–May (MAM, Fig. 2b) to September–November (SON, Fig. 2d). The corresponding seasonal departures in GODAS (not shown) give very similar patterns. Moreover, our result is qualitatively similar to the JJA pattern of the AMOC seasonal departure shown by Sime et al. (2006) from an ocean

Fig. 1 The AMOC stream function from **a** a 335-year simulation from the NCEP CFS and **b** the ocean analysis for 1979–2004 from the NCEP GODAS. The contour interval for **(a)** and **(b)** is 2 Sverdrup (Sv, or $10^6 \text{ m}^3/\text{s}$) with zero lines omitted. *Positive values* indicate clockwise circulation. **c** Shows their difference with **(a)** minus **(b)**. The contour interval for **(c)** is 1 Sv with zero lines omitted

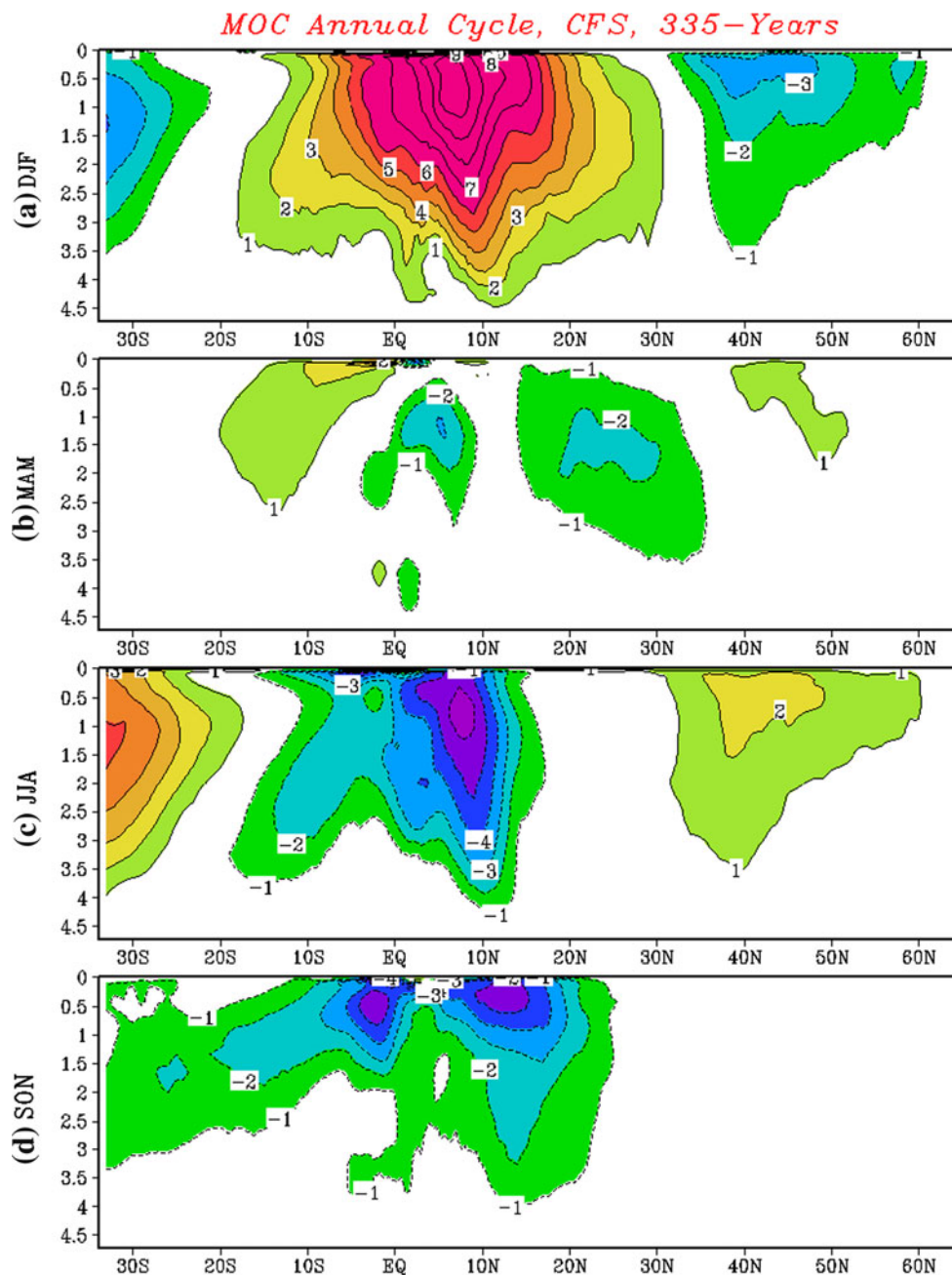
Mean Atlantic Meridional Overturning Streamfunction (Sv)



model simulation. Finally, the AMOC annual cycle in the CFS roughly corresponds to the observed seasonal volume transport variability based on the RAPID-MOCHA array at 26.5°N from 2004 to 2007, with minima in MAM and peaks appearing from late fall to winter, causing an abrupt decrease from winter to spring but a more gradual recovery into late fall (Johns et al. 2011; their Fig. 12). The spatial patterns shown in Fig. 2 imply that the major cause of the seasonal overturning departures is the Ekman transport in response to the seasonal cycle of the zonally averaged surface zonal wind stress, as demonstrated by the decomposition of Sime et al. (2006).

For variations on time scales longer than the seasonal cycle, we have applied the multi-channel singular spectrum analysis (MSSA, see a review by Ghil et al. 2002) to identify the major modes of overturning. Here we generally follow the procedure outlined by Moron et al. (1998). The MSSA obtains eigenvalues of the lag-covariance matrix for the anomalous overturning stream function with a chosen maximum lag M . For a given eigenvalue, the corresponding eigenvector forms a lag-sequence of spatial fields while the projections of the eigenvector onto the dataset constitute its time series. Though similar to the empirical orthogonal function (EOF) analysis in formulation, which corresponds

Fig. 2 The departure of the seasonal climatology of the meridional overturning stream function from its annual mean averaged for **a** December–January–February (DJF), **b** March–April–May (MAM), **c** June–July–August (JJA) and **d** September–October–November (SON). The contour interval is 1 Sv with the zero line omitted



to $M = 0$, the MSSA allows the identification of propagating oscillations as degenerate pairs of eigenmodes, having close eigenvalues and similar spatio-temporal structures except for an orthogonality in phase. Applied to the seasonally averaged data with a range of suitable values of M , the first two eigenmodes of the MSSA consistently form a degenerate pair, which corresponds to a 5-year oscillation with southward propagation of a sequence of positive and negative overturning cells of full depth from the northern subtropical to the southern equatorial Atlantic Ocean (not shown). This interannual oscillation is highly correlated with the contemporary El Niño/Southern Oscillation (ENSO) cycle. There is evidence that it is generated by the Ekman transport of the ENSO-induced surface wind anomalies over the Atlantic in the CFS.

We would like to point out that the CFS-simulated AMOC variability, though vigorous on seasonal and interannual time scales, which are largely wind driven, is expected to be weaker on multidecadal time scales due to the lack of anomalous sea ice variability and freshwater exchange with the Arctic Ocean in the model. Especially, it has been demonstrated in other models that the lower frequency band of the multidecadal variability is partly attributed to the influences of the sea ice and salinity (Frankcombe et al. 2010). Therefore, it is interesting to examine the characteristics of the lower frequency variation of the AMOC in the CFS, which is mainly driven by the temperature anomalies. Also, this gives us an opportunity to examine the mechanisms of the multidecadal fluctuations associated with ocean temperature anomalies in mid-latitudes by largely excluding the influence of the salinity change due to sea ice fluctuations.

3 AMOC multidecadal variability

To derive the leading modes of the multidecadal AMOC variability, we apply the MSSA to the annually averaged overturning stream function anomalies. To eliminate a mild climate drift in the deep ocean, the overturning stream functions are first detrended by subtracting a quadratic least-square fit at each grid point. A 5-year running mean is also applied to smooth out the major interannual fluctuations discussed in last section. Then the MSSA is carried out with a range of maximum lags M from 10 to 60 years at a 10-year increment. In all of these cases, the first eigenmode, which explains the highest percentage of the total variance, represents a stationary variation of nearly 300 years. Since its time scale is outside the range of multidecadal variability, the characteristics of this mode will be described only briefly later. On the other hand, the 2nd and 3rd eigenmodes form a degenerate pair and represent an oscillation with the dominant period around 30 years for $M \geq 20$. We choose to

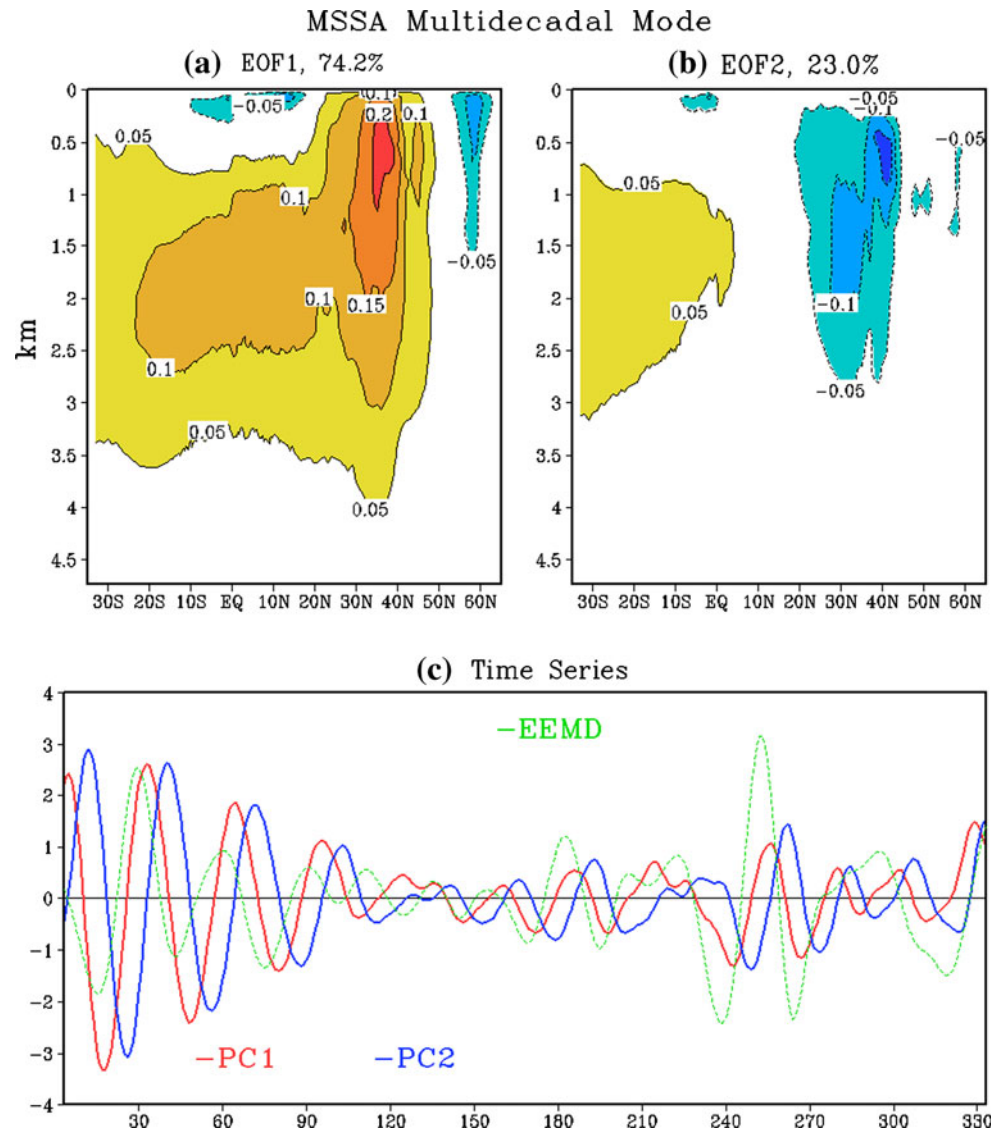
present this oscillatory mode with $M = 30$ years, which is a compromise between resolving the oscillation and preserving its instantaneous characteristics.

This propagating oscillatory mode characterized by the 2nd and 3rd MSSA eigenmodes together accounts for 14% (7.6% plus 6.4%) of the total variance. The closeness of their eigenvalues suggests that the two eigenmodes form a degenerate pair, which has been confirmed by eigenmodes at larger values of M . Following the procedure of Plaut and Vautard (1994), the oscillation mode is reconstructed based on these two eigenmodes as the filtered space–time series of the same dimensions as the original data. In this way, the characteristics of the oscillation can then be represented economically by the two leading EOF modes of the filtered data, as shown in Fig. 3.

The 1st EOF of the filtered data (Fig. 3a) explains 74.2% of the total variance of the filtered fields. Its spatial pattern is characterized by a relatively deep anomalous overturning cell centered near 40°N at depth below 500 m. Though the cell extends to great depth, at mid-latitudes most of the flow in the top limb of the cell is confined to the top 100 m or so, a point we will return to in Sect. 4.1. This overturning cell extends into the tropical and southern Atlantic at deeper levels between 1,000 and 3,000 m. It is accompanied by a shallow negative overturning cell between 10°S and 20°N above 500 m and a deeper but weaker negative cell to the north. The 2nd EOF mode (Fig. 3b), which explains 23% of the total variance, is characterized by a negative cell around 40°N while the positive and negative anomalies remain in the subtropical ocean in the lower and upper layers respectively. The principal components (PC1 and PC2) of these two EOFs show similar variations and have a clear 90° phase shift, as expected from an oscillation (Fig. 3c). This oscillation has a dominant period of 30 years and is intermittent in nature. Their magnitudes are large in the first one hundred years but gradually decrease and become very weak in the next hundred years. The oscillation is re-enhanced between Years 220 and 270 and seems to be reviving again near the end of the run.

To verify the existence of this multidecadal oscillation as identified by the MSSA, we have conducted an independent analysis of the AMOC index, which is defined as the maximum AMOC annual mean northward transport to the north of 40°N in 300–3,000 m, reflecting the fluctuation of the AMOC center in the North Atlantic (Fig. 1a). The time series has a standard deviation of 0.9 Sv and is composed of variations on a variety of time scales (black curve, Fig. 4a). We have separated the variations based on their time scales using the ensemble empirical mode decomposition (EEMD, Wu and Huang 2009). Unlike Fourier transform-based time series analysis, which uses a priori “global” basis functions of rigid periods, the method of empirical mode decomposition (EMD)

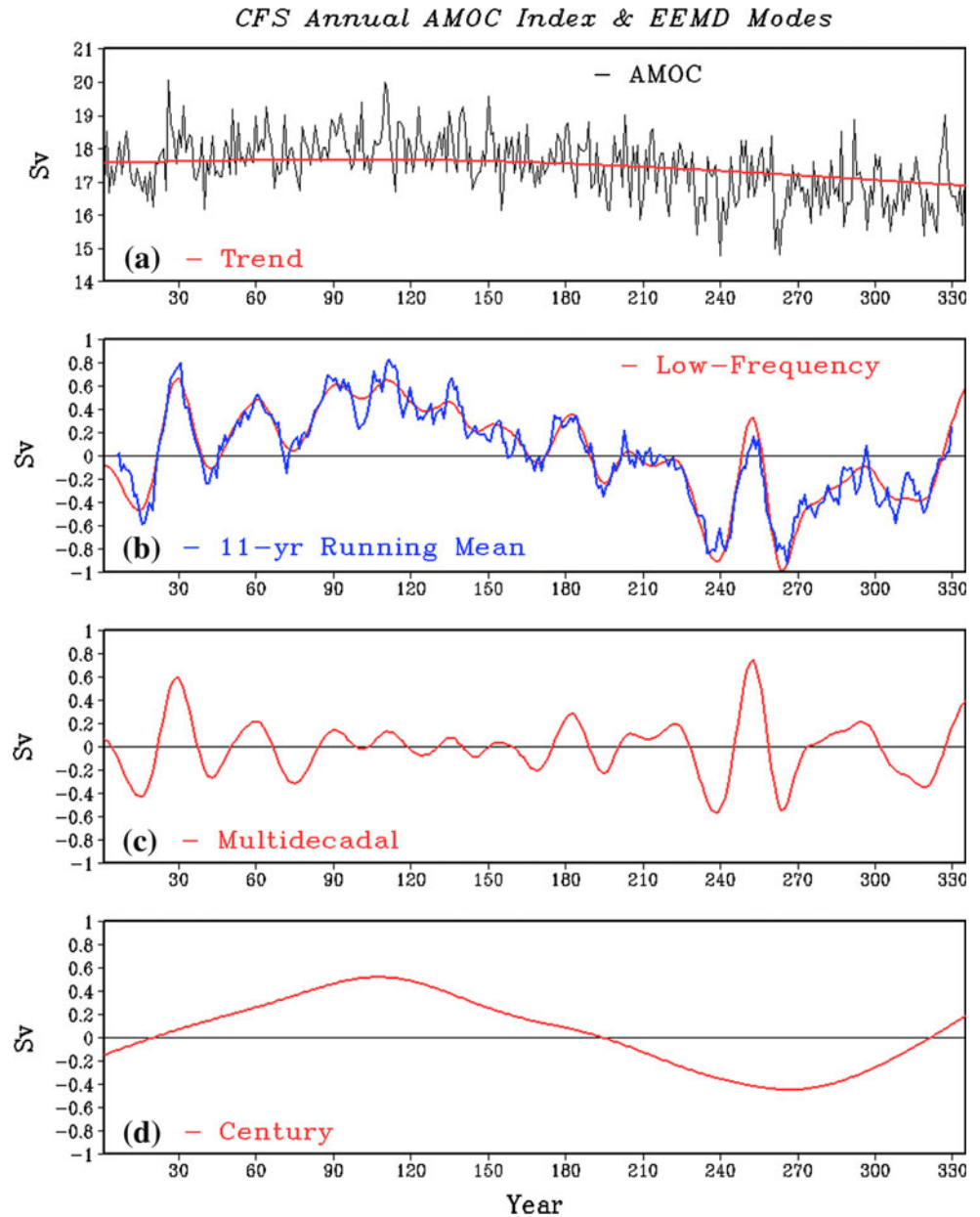
Fig. 3 **a** The spatial pattern of the 1st EOF mode of the reconstructed AMOC multidecadal mode based on the degenerate pair of the 2nd and 3rd MSSA eigenmode of the 5-year running mean Atlantic meridional overturning stream function, which together explain about 14% of total variance for the 5-year running mean data. **b** Shows the pattern of the 2nd EOF mode. The contour interval in **(a)** and **(b)** is 0.05 Sv with zero lines omitted. Their corresponding principal components (PCs) are shown in **(c)** with the *solid red curve* for the PC1 and the *solid blue curve* for the PC2. The *dashed green curve* in **(c)** represents the multidecadal mode of the EEMD analysis of the annual averaged AMOC index. The PCs and the EEMD mode are normalized



decomposes a complicated time-series into a relatively small collection of empirically determined intrinsic mode functions (IMF) based on the local characteristic time scale of the data, usually leading to easier physical interpretations (Huang et al. 1998). More recently, the EEMD technique was developed to improve the robustness of the decomposition. In the EEMD, multiple noise realizations are added to the single observed time series, mimicking a scenario of multiple experimental trials with inherent uncertainty. The ensemble average is used to derive the corresponding IMFs (Wu and Huang 2009). It has been shown that the EEMD extracts scale-consistent signals and makes the IMFs less dependent on the sample size. More detailed descriptions of the method can be found in Huang and Wu (2008) and Wu and Huang (2009). This method has been used to analyze various climate phenomena (e.g., Wu et al. 2011; Huang et al. 2011a; Hu et al. 2011).

The intrinsic mode functions derived from the AMOC index can be easily categorized into the interannual, decadal, multidecadal, and century components based on their time scales. A nonlinear trend is also identified as a part of the EEMD, which is shown as the red curve in Fig. 4a. In this study, we concentrate on the multidecadal and century components and refer them collectively as the low-frequency signals. This low-frequency AMOC index derived from the EEMD analysis (red curve, Fig. 4b) shows significant fluctuations that are very similar to the detrended 11-year running mean of the original annual AMOC index (blue curve). It has a standard deviation of 0.4 Sv with maximum magnitude of 1 Sv and accounts for 20% of the total variance of the original index. This confirms that the CFS still generates substantial AMOC fluctuations on multidecadal and longer time scales although there is no active sea ice and freshwater exchange with the Arctic Ocean in the model.

Fig. 4 **a** The annual mean AMOC index (the black curve) and its long-term trend from the EEMD analysis. **b** Low frequency AMOC index (red curve) as the sum of the EEMD multidecadal and century components of the EEMD modes. This EEMD low-frequency index is similar to the 11-year running mean of the detrended original AMOC index (blue curve). **c** The EEMD multidecadal component of the AMOC index. **d** The EEMD century component of the AMOC index



The multidecadal EEMD component shows an intermittent oscillation with a dominant period of about 30 years (Fig. 4c), which is prominent in the first 100-year and around the years 210–270 of the simulation but relatively weak in between. The century EEMD component shows a long period of near 300 years (Fig. 4d). To further demonstrate the relationship between the original AMOC index and its EEMD components, Fig. 5a shows the power spectra of the annual mean AMOC index and the two low-frequency EEMD components. The nonlinear trend (the red curve in Fig. 4a) is removed from the total AMOC index before the spectral analysis. In the low-frequency band, the power spectrum of the AMOC index shows two distinctive peaks centered near the periods of 30 and 300 years

respectively (blue curve, Fig. 5a). On the other hand, the spectrum of the multidecadal (century) EEMD component peaks at the period of 30 (300) years as shown in the red (green) curve in Fig. 5a, which is also consistent with the temporal characteristics demonstrated in Fig. 4c (Fig. 4d). The fact that the power spectral peaks of the AMOC index closely match those of the EEMD time series suggests that the EEMD modes are representative of the AMOC variations with the respective characteristic time scales.

We notice that the peak of the quasi 30-year oscillation in the spectrum of the AMOC index is below the level of the corresponding red noise spectrum (dashed black curve), which weakens our claim that the AMOC index has a distinctive oscillation on the 30-year time scales somewhat.

On the other hand, we argue that some technical factors may contribute to this. First, the high intermittency of the quasi 30-year oscillation, as the EEMD time series shows, may cause its under-representation in a power spectrum, which is most efficient in measuring stationary processes (e.g., Huang and Wu 2008). Second, comparing the structures of the spectra of the AMOC index (blue curve) and red noise (dashed black curve) shown in Fig. 5a, it is possible that red noise may not be the most suitable background for the spectrum of the AMOC index. In fact, the slope of the spectrum of the AMOC index clearly deviates from that of a red noise spectrum in low frequencies, although it is roughly consistent with the red noise in the interannual-to-decadadal band. We suspect that these factors may partly be why the local 30-year peak does not pass the significance level of red noise. The existence of local peaks in both spectra of the original and EEMD indices, however, suggest that our statistical methods, both the MSSA and EEMD, identify the intermittent quasi 30-year fluctuation as a physical entity, instead of an artifact of band filtering.

To further demonstrate the intermittency of the quasi 30-year oscillation, we have conducted a wavelet analysis of the annual mean AMOC index with its trend removed, following the procedure of Hu and Nitta (1996). The wavelet transform (Fig. 5b) shows that the multidecadal AMOC fluctuation has larger amplitude in the frequency

band centered at 30-year period in the first 100 years of the simulation and again between 210 and 270 years. The amplitudes, however, are much weaker between these two episodes. This result is consistent with those derived independent from the EEMD analysis and further verifies the validity of characterizing the AMOC multidecadal variations as an intermittent quasi 30-year oscillation.

Moreover, the temporal characteristics of the multidecadal EEMD component are generally consistent with the independently derived propagating MSSA mode discussed above. In fact, the green curve in Fig. 3c is the normalized version of the EEMD multidecadal component (Fig. 4c), which shows a fixed phase relation with both the PC1 and PC2 when their amplitudes are relatively large. The maximum transport (i.e., the EEMD time series) leads the PC1 by a quarter of the period most of the time and is nearly out-of-phase with PC2. It is interesting to see that the EEMD shows more distinctive signals in the second major epoch of the oscillation during the years 210–270. This suggests that the EEMD is more effective in delineating the intermittent signals of short duration.

The EEMD century component (Fig. 4d) is largely consistent with the dominant time variation of the 1st MSSA eigenmode, as shown by its near in-phase relation with the PC1 of the reconstructed fields (Fig. 6b). The EOF1 (Fig. 6a) shows a basin-wide strengthening and

Fig. 5 **a** The power spectrum of the annual mean AMOC index with its nonlinear trend removed (*blue curve*) and its corresponding *red noise* spectrum (*dashed black curve*). The *red (green)* curve shows the power spectrum of the multidecadal (century) EEMD components. **b** The wavelet transform of the annual mean AMOC index with its nonlinear trend removed

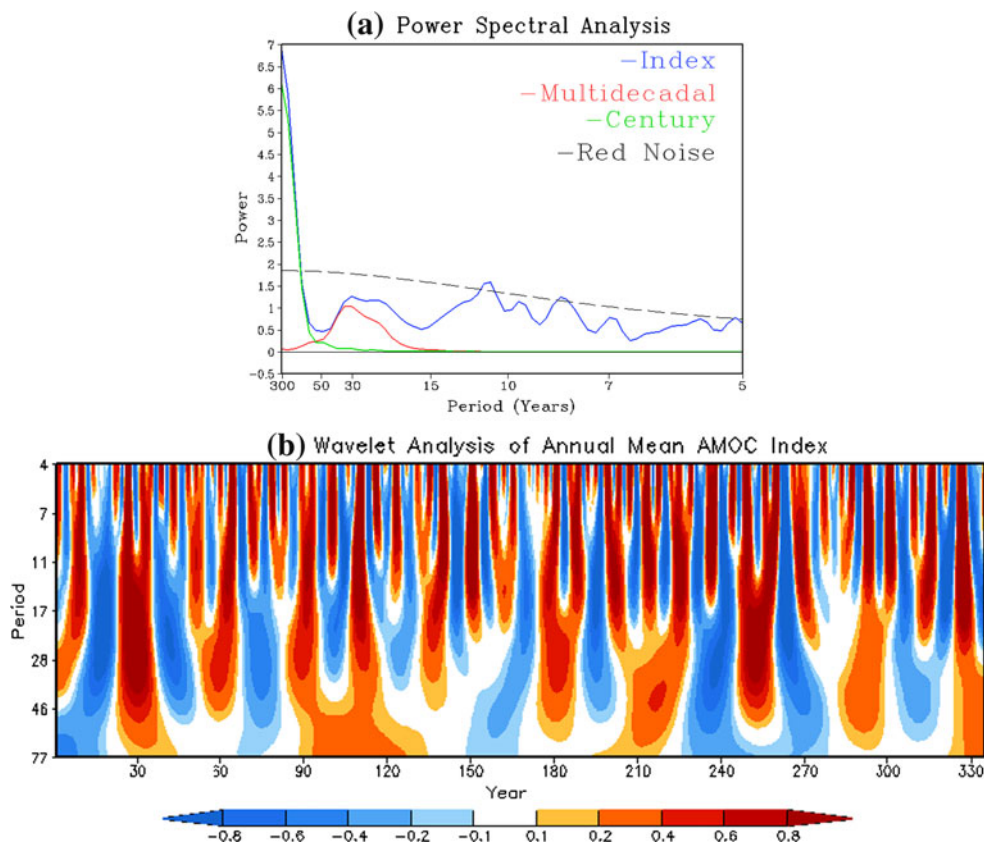
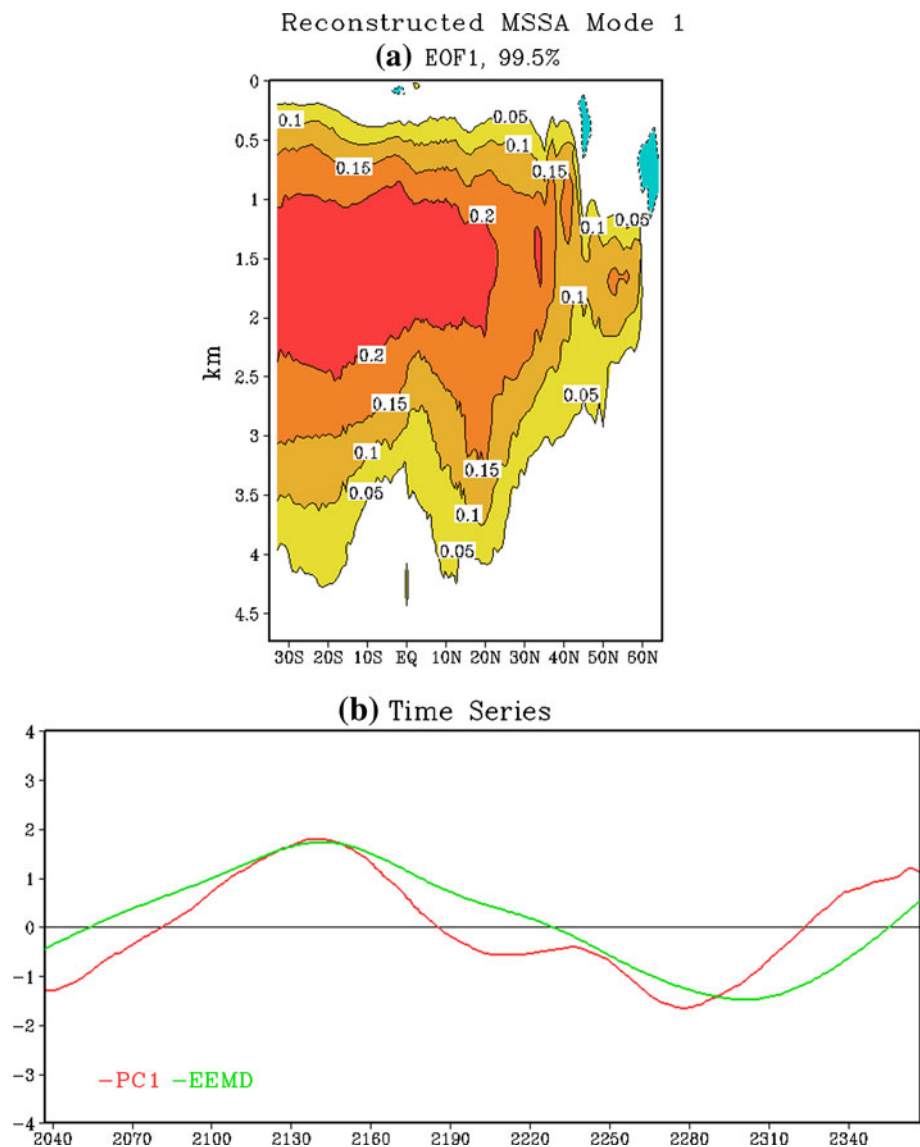


Fig. 6 **a** The spatial pattern of the 1st EOF mode of the reconstructed AMOC centennial mode based on the 1st MSSA eigen mode of the 5-year running mean Atlantic meridional overturning stream function, which explains about 22% of total variance and represents the long stationary oscillation of 300 years. The contour interval in **(a)** is 0.05 Sv with zero lines omitted. The corresponding principal component (PC) is shown in **(b)** with the *red curve* for the EOF1. The *green curve* in **(b)** represents the century mode of the EEMD analysis of the annual averaged AMOC index. The PC and the EEMD mode are normalized



weakening of the AMOC on century time scales. Overall, the similarity between the MSSA and EEMD is reassuring and confirms the robustness of these modes.

4 Composite lifecycle

In this section, we use the phase-compositing technique described by Plaut and Vautard (1994) and Moron et al. (1998) to examine the evolution of the multidecadal oscillation within a complete cycle. This evolution can be measured by a phase index calculated from the PC1 (Fig. 3c) of the reconstructed space–time series, following Moron et al. (1998), which varies from 0 to 2π within each cycle. Averaging model variables over intervals in the phase index that are $\pi/4$ long for all cycles produces a composite oscillation composed of 8 averages, which we

refer to as the eight phases of the lifecycle. Since the period of the oscillation is around 30 years, each of these phase composites represents an averaging period of roughly 4 years. The composites are based on the 5-year running mean data for all variables. We use first 100-year data to construct the composites because this is the period in which the intermittent oscillation is strongest and the phase increase within each cycle is monotonic. The other active episode of the oscillation, from years 210 to 270, also shows similar features. The lifecycles of several key variables are described below.

4.1 Overturning anomaly

The multidecadal overturning anomaly is characterized by a “deep” overturning anomaly which reaches depths of a few kilometers, and a “shallow subtropical” overturning

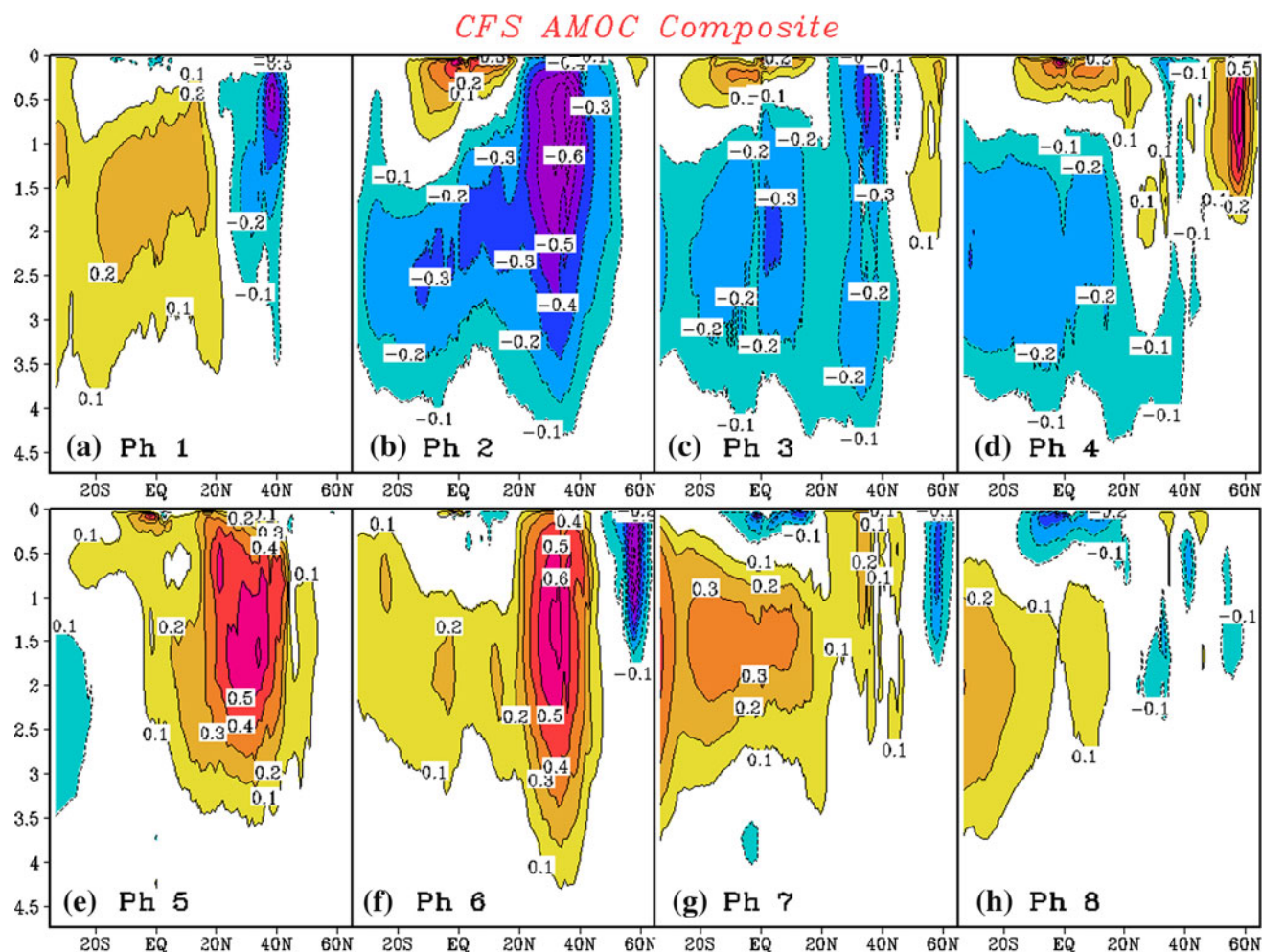


Fig. 7 The lifecycle composite of the AMOC oscillation at a period around 30 years based on the 2nd and 3rd MSA modes of 5 year running mean AMOC shown in Fig. 3c for **a** Phase 1, **b** Phase 2, **c** Phase 3, **d** Phase 4, **e** Phase 5, **f** Phase 6, **g** Phase 7 and **h** Phase 8. Each phase of the composite is averaged from the corresponding

phases of major episodes in the first hundred years. The contour interval is 0.1 Sv with zero contours omitted. The composite is constructed using the total anomalies of the 5 year running mean AMOC stream function

anomaly in the top few hundred meters (Fig. 7). The amplitudes of the overturning structures are about 0.6 Sv for the deep anomaly and more than 0.3–0.4 Sv for the shallow subtropical anomaly.

Each deep overturning anomaly starts in the north and grows southward while coexisting with, and eventually replacing, the opposite anomaly. The positive (northern-downwelling) phase of the deep anomaly begins at around 50°N during Phase 2 (Fig. 7b) and strengthens at the same location until Phase 4 (Fig. 7c, d). The center of the cell then moves southward to about 35°N (Fig. 7e). During this time, the top of the overturning anomaly is at the surface and its bottom reaches 3,000 m. By Phase 6 (Fig. 7f) the positive anomaly extends into the southern hemisphere; in the extension, the top of the overturning occurs below about 500 m depth. During Phases 7 and 8, the anomaly weakens north of about 30°N (Fig. 7g, h) until only the southward

extension of the anomaly is left (Fig. 7a, h). The negative phase of the deep overturning begins at high latitudes at Phase 6 (Fig. 7f) and follows a similar evolution (Fig. 7a–d).

As mentioned in the description of the MSA EOF1 (Sect. 3 and Fig. 3a), much of the upper limb of the cell occurs in the top 100 m or so in the strongest part of the cell near 30°N. This is much shallower than the mean AMOC cell, which has an upper limb filling the top kilometer of the water column (Fig. 1a), or the century mode (Fig. 5a). Such shallow flow looks less like a typical deep overturning cell and more like an overturning associated with Ekman transport, such as the STC's or the seasonal variation in overturning (Fig. 2).

The anomaly of the shallow cell displays a simpler evolution, with a single cell between 20°S and 20°N oscillating in place (Fig. 7). The anomalous cross-equatorial shallow cell has downwelling and upwelling occurring

Composite SST Anomalies

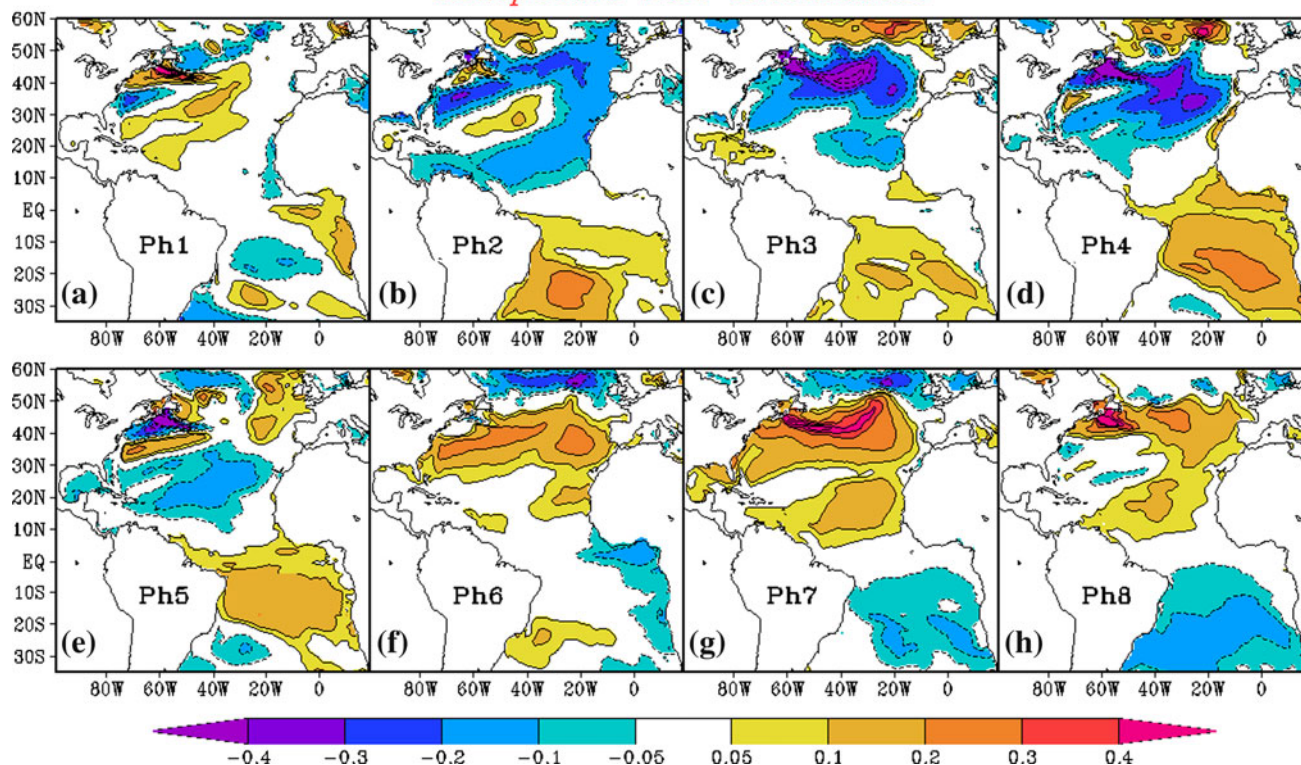


Fig. 8 The composite SSTA in the eight phases of the lifecycle of the multidecadal AMOC oscillation as shown in Fig. 7 for **a** Phase 1, **b** Phase 2, **c** Phase 3, **d** Phase 4, **e** Phase 5, **f** Phase 6, **g** Phase 7 and **h** Phase 8. The contour interval is 0.1°C for the SST anomalies, with

the zero lines omitted and the contours of $\pm 0.05^{\circ}\text{C}$ added to highlight the range of anomalies in the tropics. The maximum/minimum contours are at $\pm 0.5^{\circ}\text{C}$ respectively. The color bar for the shading is shown at the bottom

in opposite hemispheres and contrasts with the mean Subtropical Cells (STCs, McCreary and Lu 1994; Liu 1994; Schott et al. 2004). Since the anomalous shallow cell spans the domain of both STCs and apparently affects their strength, we will refer to it as the subtropical cell anomaly (STCA), noting that it has a different spatial structure from the mean STCs and affects the strength of both STCs south and north of the equator. The STCA tends to be of the opposite sign to the deep anomaly directly beneath it. On the other hand, the STCA is not exactly out of phase with the deep overturning anomaly. The positive STCA is enhanced in Phases 2–3 when the negative deep overturning dominates near 35°N and extends south of the equator (Fig. 7b, c). However, while the deep negative anomaly is weakened throughout the basin in Phase 4, the positive STCA is persistent and expands northward (Fig. 7d). As a result, the deep and shallow overturning anomalies have the same sign in Phase 5 (Fig. 7e).

4.2 SST and HCA anomalies

The AMOC oscillation is associated with a systematic evolution of SST anomalies (SSTA, Fig. 8). Mid-latitude (roughly $30^{\circ}\text{--}50^{\circ}\text{N}$) SST cools during phases 1–4 (Fig. 8a–

d), when and after the deep cell is associated with weakened northward upper-ocean volume transport (Fig. 7a–c), and warms during phases 5–8 (Fig. 8e–f), during and after strengthened upper-ocean volume transport (Fig. 7e–g). These anomalies first form near the western boundary (Fig. 8a, e) then extend eastward. The cold (Fig. 8b) and warm (Fig. 8g) mid-latitude SSTA also extend southward along the eastern boundary and westward around 10°N in a horseshoe-shape reminiscent of the observed AMO pattern (e.g., Fig. 1a of Sutton and Hodson 2007). The SSTA in the southern hemisphere tropics and in the northern hemisphere high latitudes tend to have opposite sign to the mid-latitude SSTA.

We measure subsurface temperature variation with the upper ocean heat content anomaly (HCA), defined as the ocean temperature anomaly averaged over the upper 460 m. At mid-latitudes, these show similar sign and evolution (Fig. 9) as SSTA (Fig. 8). In contrast to the horseshoe-shaped SSTA pattern (Fig. 8), the northern hemisphere HCA tends to have subtropical values with opposite sign of its mid-latitude values (Fig. 9). The southern hemisphere subtropics does not have as strong an HCA signal. Zhang (2007) has pointed out that the out-of-phase relation between the SSTA and HCA is an AMOC signature in the tropical North Atlantic.

Composite HC Anomalies

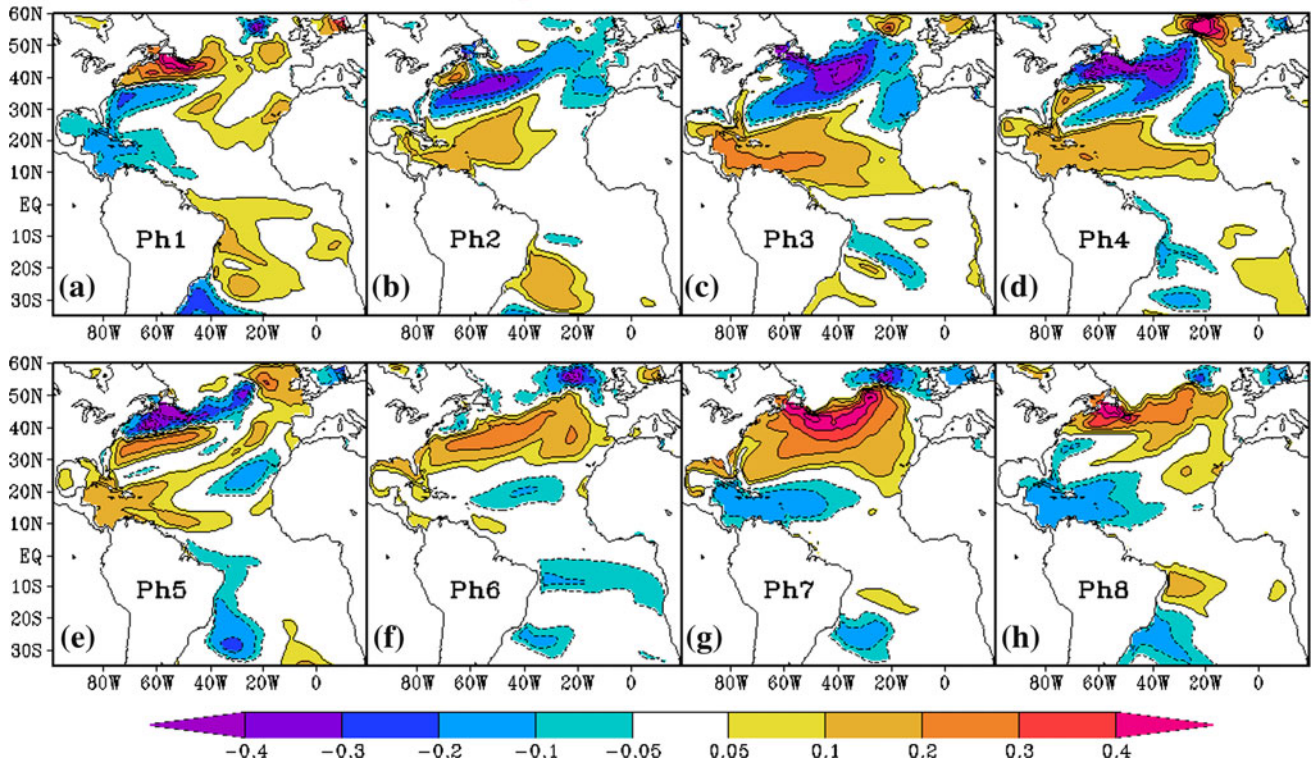


Fig. 9 The composite HCA in the eight phases of the lifecycle of the multidecadal AMOC oscillation as shown in Fig. 7 for **a** Phase 1, **b** Phase 2, **c** Phase 3, **d** Phase 4, **e** Phase 5, **f** Phase 6, **g** Phase 7 and **h** Phase 8. The contour interval is 0.1°C with the zero lines omitted

and the contours of $\pm 0.05^\circ\text{C}$ added to highlight the range of anomalies in the tropics. The maximum/minimum contours are at $\pm 0.5^\circ\text{C}$ respectively. The color bar for the shading is shown at the bottom

Fig. 10 The composite anomalous meridional heat transport in the Atlantic Ocean as a function of latitude and phase in **a** the whole depth of the ocean and **b** the upper 460 meters only. The contour interval is 10 terawatts (10^{12} Watts) with zero lines omitted

Meridional Heat Transport Composite

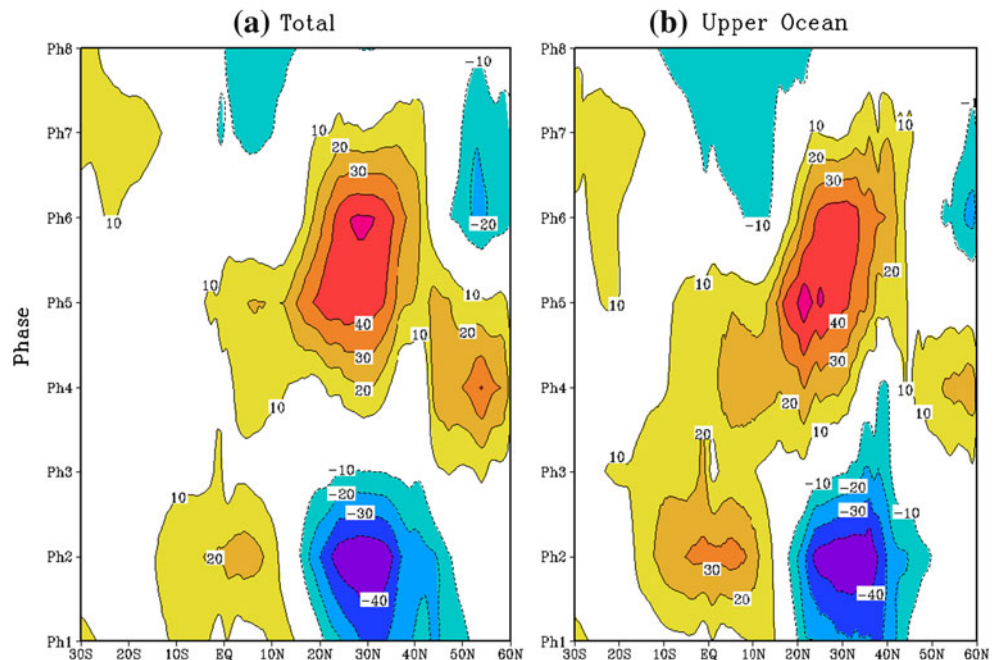
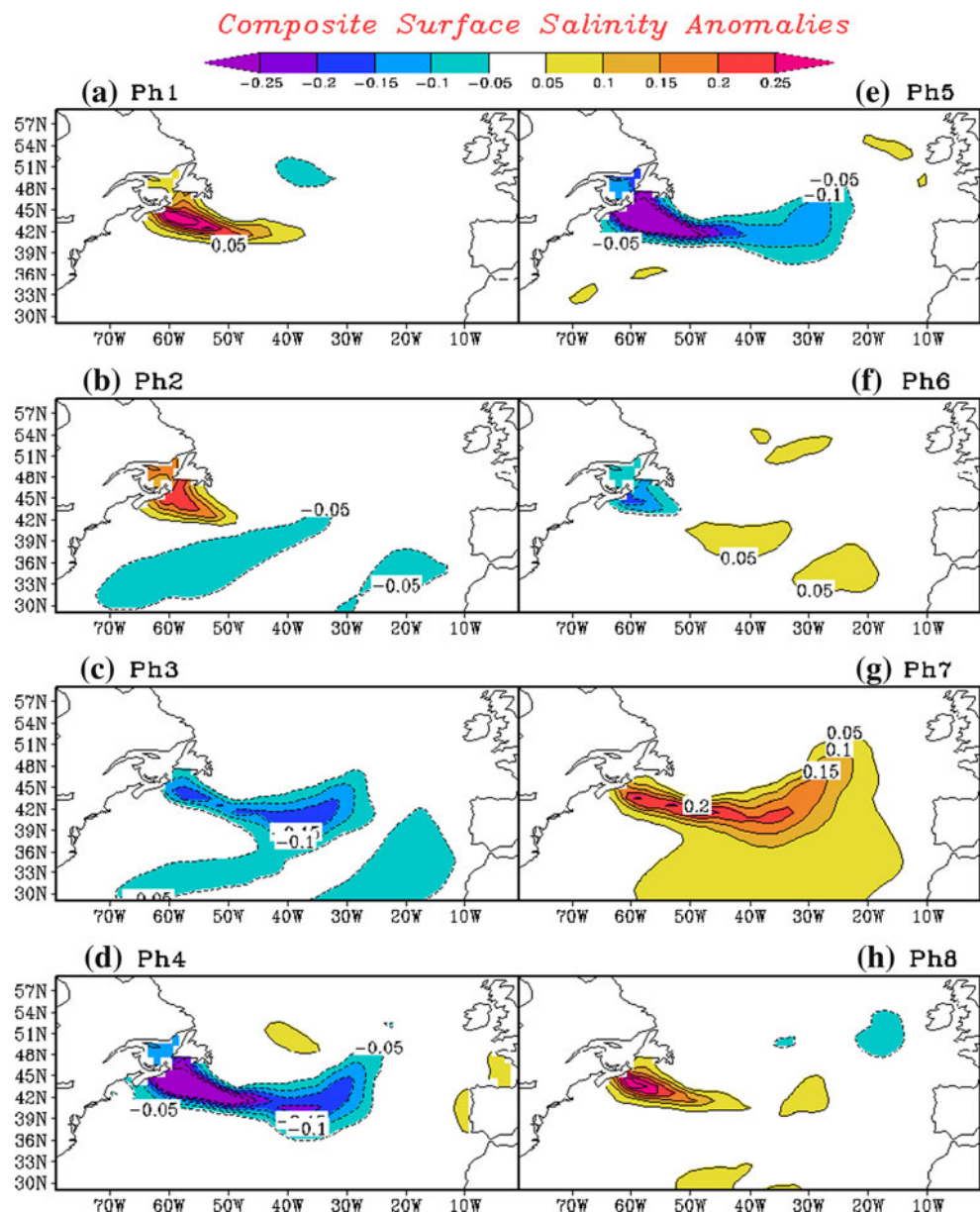


Fig. 11 The composite anomalies of the sea surface salinity in the eight phases of the lifecycle of the multidecadal AMOC oscillation as shown in Fig. 7 for **a** Phase 1, **b** Phase 2, **c** Phase 3, **d** Phase 4, **e** Phase 5, **f** Phase 6, **g** Phase 7 and **h** Phase 8. The contour interval is 0.05 psu with the zero lines omitted. The color bar for the shading is shown at the top



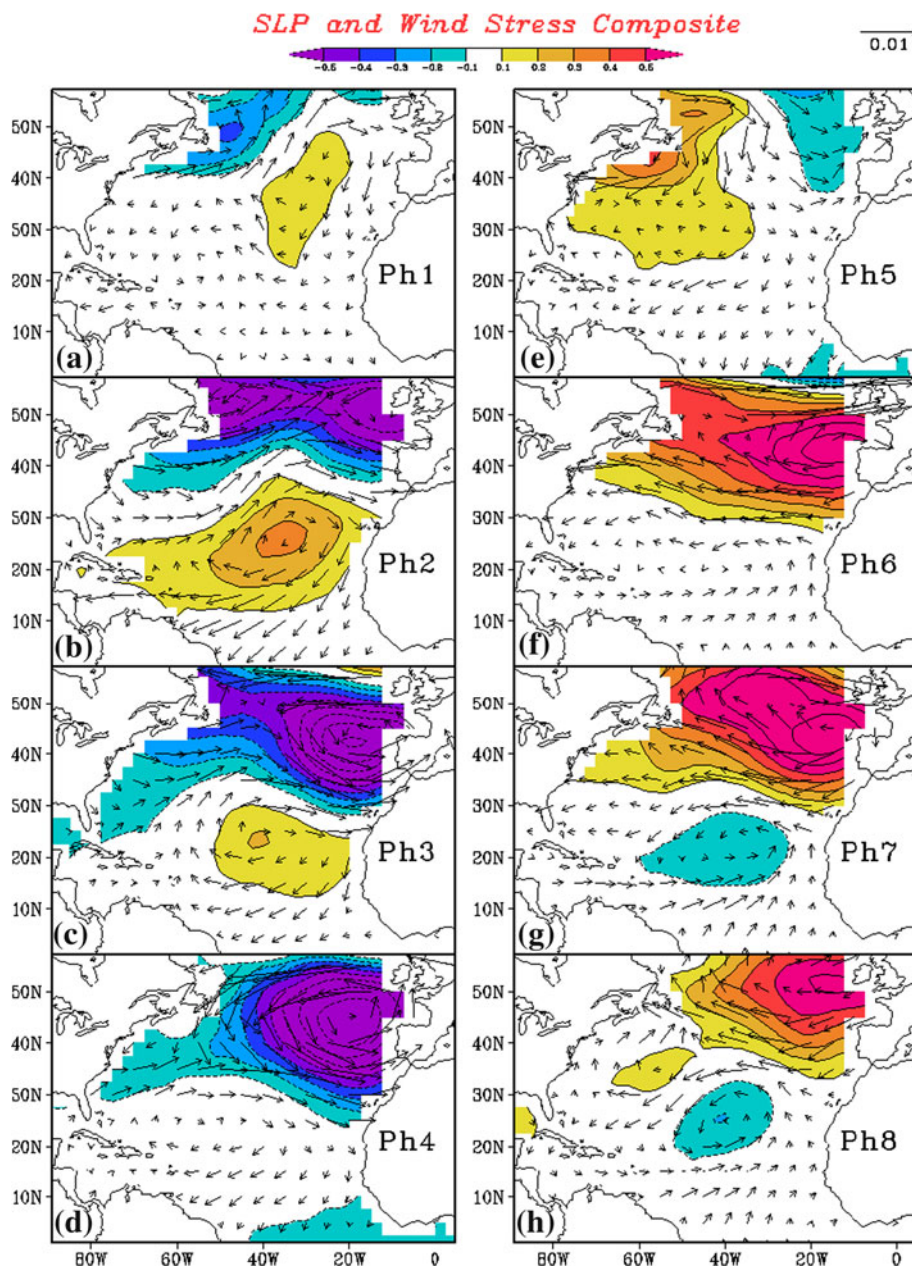
The overturning stream function anomalies (Fig. 7) may influence SSTA and HCA through meridional heat transport anomalies, which are shown as a function of latitude and phase in Fig. 10a. Negative (Fig. 7a–c) and positive (Fig. 7e–g) mid-latitude overturning anomalies are associated with the same sign anomalous northward heat transport centered at 30°N (Fig. 10a). The divergence of the anomalous northward heat transport implies cooling of the 30°N–50°N region during phases 1–3 and warming during phases 4–7, which is consistent with the HCA and SSTA evolution in that region. Between 15°N and 30°N, the anomalous northward heat transport divergence is opposite to the mid-latitude values, which is consistent with the HCA evolution in that region (warming during phases 1–3 and cooling during phases 4–7) but not the

SSTA. We argue in Sect. 5.2 that latent heat flux anomalies associated with wind speed anomalies account for the subtropical SST evolution.

4.3 SSS anomaly

We have also analyzed the fluctuation of the salinity in the AMOC multidecadal oscillation. The only region where the sea surface salinity (SSS) shows significant anomalies is around 40°N–50°N (Fig. 11) where the SSTA and HCA are also strongest (Figs. 8, 9). In general, the local cold SSTA is associated with negative SSS anomaly (SSSA) with a phase delay. While cold SSTAs prevail in the mid-latitudes from Phase 2 to 4, a nearly zonal belt of the negative SSSAs appears in the same location as the largest SSTAs

Fig. 12 The composite SLP (contour and shading) and wind stress (vector) anomalies in the eight phases of the lifecycle of the multidecadal AMOC oscillation as shown in Fig. 7 for **a** Phase 1, **b** Phase 2, **c** Phase 3, **d** Phase 4, **e** Phase 5, **f** Phase 6, **g** Phase 7 and **h** Phase 8. The contour interval is 0.1 hPa with zero lines omitted. The color bar for the shading is shown at the top center. The vector scale for 0.01 Nm^{-2} is shown at upper right

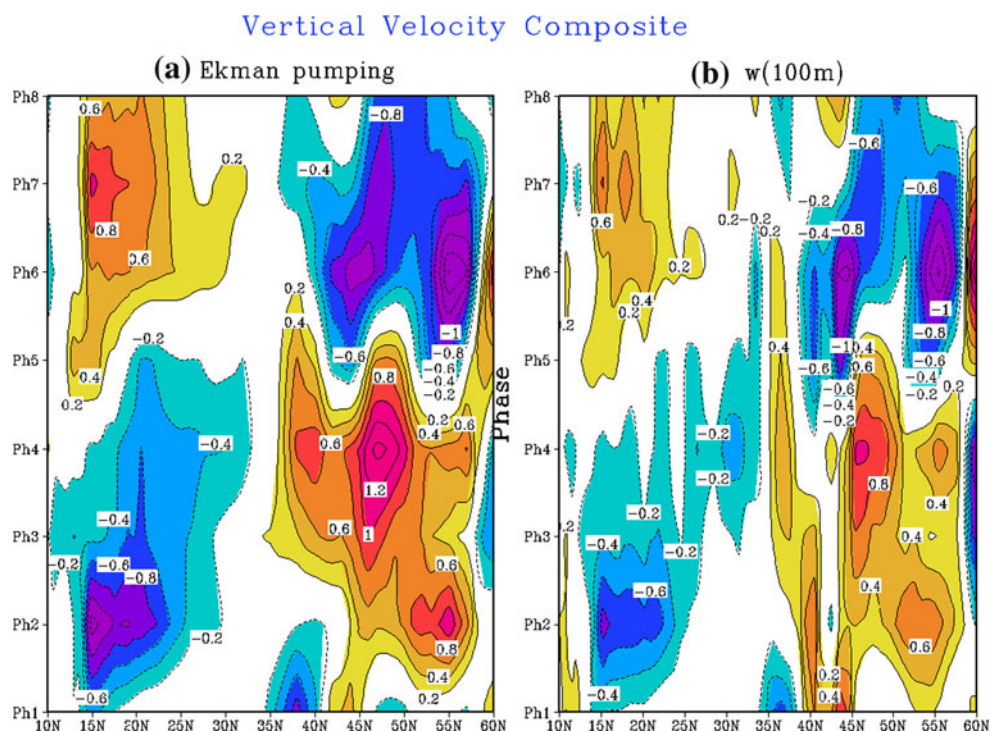


between 35°N and 45°N in Phase 3 (Fig. 11c). This belt is enhanced in the next two phases (Fig. 11d–e) then weakened in Phase 6 (Fig. 11f). A similar delayed evolution of positive SSSA with respect to the warm SSTA occurs from Phases 7–8 (Fig. 11g–h) to Phases 1–2 (Fig. 11a–b). Since the SSTA in this region is likely determined by the effect of the subsurface water, this implies that the upwelled subsurface water is fresher than the surface water in this area and the salinity tends to compensate the temperature's effect on density anomaly. The delay between the SSTA and SSSA is consistent with previous results from Delworth et al. (1993) and suggests that the advection by the gyre circulation affects the SSSA distribution.

4.4 SLP and wind stress anomalies

The AMOC multidecadal oscillation is closely associated with sea level pressure (SLP) and wind stress (Fig. 12) anomalies. In mid-latitudes, a cyclonic circulation anomaly around a center of low SLP anomaly (SLPA) appears in phases 2–4 (Fig. 12b–d), while an anticyclonic, high SLPA center appears in phases 6–8 (Fig. 12f–h). The anticyclone and cyclone are associated with cold (Fig. 8b–d) and warm (Fig. 8f–h) mid-latitude SSTA, respectively. Like the SSTAs, the wind and SLPA tend to extend eastward from the western Atlantic and form major centers of the SLPA and circulation near the eastern boundary between 40° and

Fig. 13 The zonally averaged **a** Ekman pumping and **b** the vertical velocity at 100 m in the Atlantic basin from 10°N to 60°N for the eight phases of the composite AMOC multidecadal lifecycle. The contour interval is 0.2 cm day⁻¹ with zero lines omitted



50°N in their peaks. These surface atmospheric circulation anomalies may be seen as a response of the lower atmosphere to the anomalous SST gradient (e.g., Lindzen and Nigam 1987). An additional atmospheric circulation anomaly is centered at about 20°N and tends to have the opposite circulation direction to the mid-latitude anomaly. The potential mechanism of this STC will be discussed in Sect. 5.2.

Overall, we have established that the 30-year oscillation of the overturning stream function includes changes in both the deep overturning in the mid-latitude Atlantic and the shallow overturning in the subtropics with a fixed phase relationship. It is also associated with the systematic fluctuations of the SST and upper ocean heat content in the extratropical and tropical Atlantic, as well as the SSS in the mid-latitudes. The corresponding atmospheric fluctuations suggest that the interactions between the atmosphere and ocean are possibly an important component of the process. The potential mechanisms that generate these connections among different variables and cause the oscillation will be discussed in the next section.

5 Potential feedback mechanisms

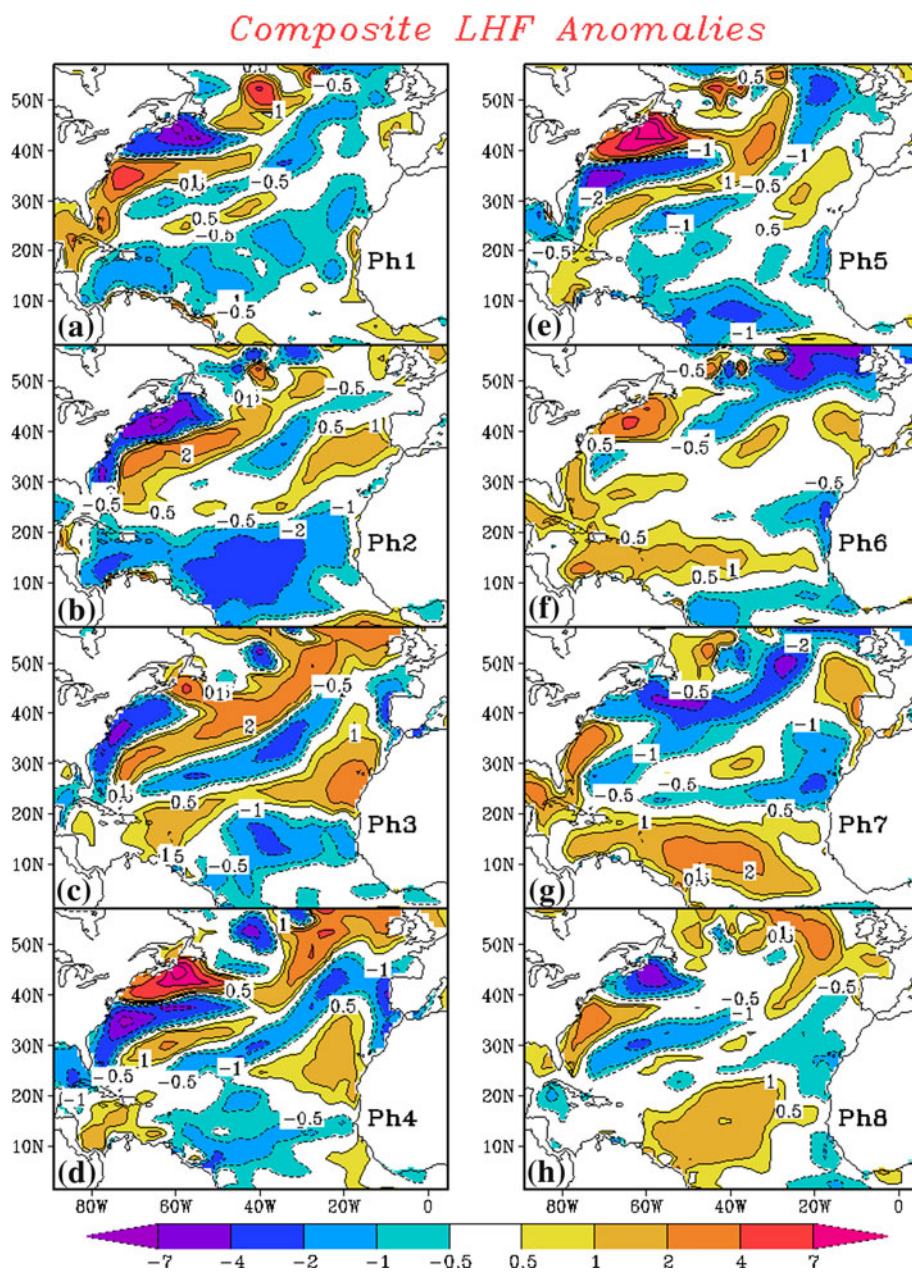
In Sect. 4, we have shown the multidecadal AMOC variation in the CFS as an oscillatory fluctuation around its climatology with a quasi-period of 30 years. Physically, an oscillation is a periodical movement around its equilibrium

state caused by a net restoring force, which grows stronger as the system deviates away from the equilibrium state. The period of oscillation is determined by the strength of the net restoring force. In a climate system, such net restoring force can be generated by the combination of a positive feedback and a delayed negative one, such as the delayed oscillator mechanism for ENSO (e.g., Schopf and Suarez 1988; Suarez and Schopf 1988). In this section, we provide some evidence to show that the combined effect of a positive and a delayed negative feedback may be responsible for the quasi 30-year oscillation in the CFS.

5.1 Positive feedback in mid-latitudes

A positive feedback between the ocean and atmosphere may occur in the mid-latitudes, which sustains the anomalies of deep overturning. Surface wind anomalies (Fig. 12) drive ocean Ekman upwelling and downwelling anomalies beneath cyclones and anticyclones, respectively. The wind-induced vertical movement is most clearly seen in the zonally averaged Ekman pumping as a function of latitude and phase of the composite lifecycle (Fig. 13a). In the mid-latitudes, the Ekman upwelling (downwelling) starts between 50°N and 55°N in Phase 2 (Phase 6) and then expands equatorward, consistent with the enhancement of the negative (positive) deep overturning cell. This dominant effect of the Ekman pumping is confirmed by the composite vertical velocity at 100 m, which shows a pattern (Fig. 13b) qualitatively similar to Fig. 13a with

Fig. 14 The composite anomalies of the surface latent heat flux corresponding to the phases of the lifecycle of the multidecadal AMOC oscillation as shown in Fig. 7 for **a** Phase 1, **b** Phase 2, **c** Phase 3, **d** Phase 4, **e** Phase 5, **f** Phase 6, **g** Phase 7 and **h** Phase 8. Positive values represent heat flux into the ocean. The contours are drawn at ± 0.5 , ± 1.0 , ± 2.0 , ± 4.0 , ± 7.0 and $\pm 10.0 \text{ Wm}^{-2}$ with the zero lines omitted. The color bar for the shading is shown at the bottom



comparable magnitude. The composites of the vertical velocities at other model levels in the upper ocean (50, 200, and 303 m) give similar patterns to that at 100 m.

In Subsect. 4.4, we have argued that the wind and hence the Ekman pumping anomalies are responses to the SSTA in mid-latitudes. Furthermore, we have also shown that the SSTA in the mid-latitudes are largely induced by the HCA, which is in turn a response to the meridional heat transport by the anomalous deep overturning. Therefore, we suggest that the wind-induced enhancement of the deep overturning anomalies tend to sustain the mid-latitude HCA and SSTA patterns. These processes then form a positive feedback loop in the mid-latitude ocean–atmosphere interactions.

We have also examined the surface latent heat flux anomalies (Fig. 14), which are usually a major factor to generate mid-latitude SSTA. In this case, however, we do not see a close association between the spatial patterns of the latent heat flux anomalies and the SSTA in the mid-latitudes. Especially, during Phases 3–4, when the negative SSTA is largest between 40°N and 50°N (Fig. 8c–d), the latent heat flux anomalies are generally positive (Fig. 14c–d) and tend to damp out the SSTA. A similar relationship occurs during Phases 7–8, when the SSTA is generally positive in mid-latitudes. Therefore, we suggest that the SSTA is mainly caused by the HCA, instead of the surface heat flux. The surface heat flux, however, plays a major

role in generating the SSTA in the tropics, to be described in the next subsection.

5.2 Negative feedback from subtropics

The negative feedback involves the interactions between the tropical and mid-latitude variations and explains the out-of-phase relationship between the subtropical SSTA and HCA, as well as the fluctuation of the STCA.

First, the AMOC-induced SSTA, once established in the mid-latitudes, tends to expand into the subtropics through the coupled WES interaction among the surface wind, evaporation and SST. For instance, as the negative SLPA is established in the mid-latitudes in Phase 2, a positive SLPA center is developed at 25°N, enhancing the subtropical high and the southeast trade winds to its south (e.g., Fig. 12b). The stronger wind speeds between the equator and 20°N induce substantial loss of latent heat from the sea surface from Phase 1 to 5 (Fig. 14a–e), which are largest in Phase 2 (Fig. 14b). This heat loss is the main reason for the cooling of the SST in the tropical region during Phases 2–5 (Fig. 8b–e). A similar relationship holds between the warm SSTAs (Fig. 8f–h), weakened northeast trades (Fig. 12f–h), and positive latent heat flux anomalies in the tropics during the Phases 6–8 (Fig. 14f–h). The WES interaction expands the mid-latitude SSTA into the tropical Atlantic through a coupled process, as described in previous studies (e.g., Dahl et al. 2005; Chiang et al. 2008; Mahajan et al. 2010).

The AMOC-induced tropical wind anomalies also cause oceanic dynamical responses. The subtropical surface wind stress anomalies described above form an anticyclone in Phases 2–5 (Fig. 12b–e) and a cyclone in Phases 6–8 (Fig. 12f–h). These wind stress anomalies force Ekman pumping centered at 15°N–20°N, with downwelling in Phases 2–4 and upwelling in Phases 6–8 (Fig. 13a), which are the major signals in the upper ocean vertical velocity (Fig. 13b). The tropical vertical velocity anomalies are generally out-of-phase with the extratropical ones. In the tropical Atlantic, the downwelling generates warm HCA during Phases 2–5 (Fig. 9b–e) while the upwelling causes cold HCAs during Phases 6–8 (Fig. 9f–h). These subtropical HCAs have opposite signs to the subtropical SSTAs and the mid-latitude HCAs. After the generation, the warm HCAs are generally enhanced at the western boundary in lower latitudes (Fig. 9c), then propagate northward along the coast (Fig. 9d) and form a warm HCA belt between 30°N and 40°N (Fig. 9e), which reduces the cold HCAs in the mid-latitudes. A similar cold HCA largely follows the same propagation route.

The tropical HCAs correspond closely to the development of the STCA shown in Fig. 7. In general, the warm HCA (Fig. 9b–e) is associated with the positive STCA

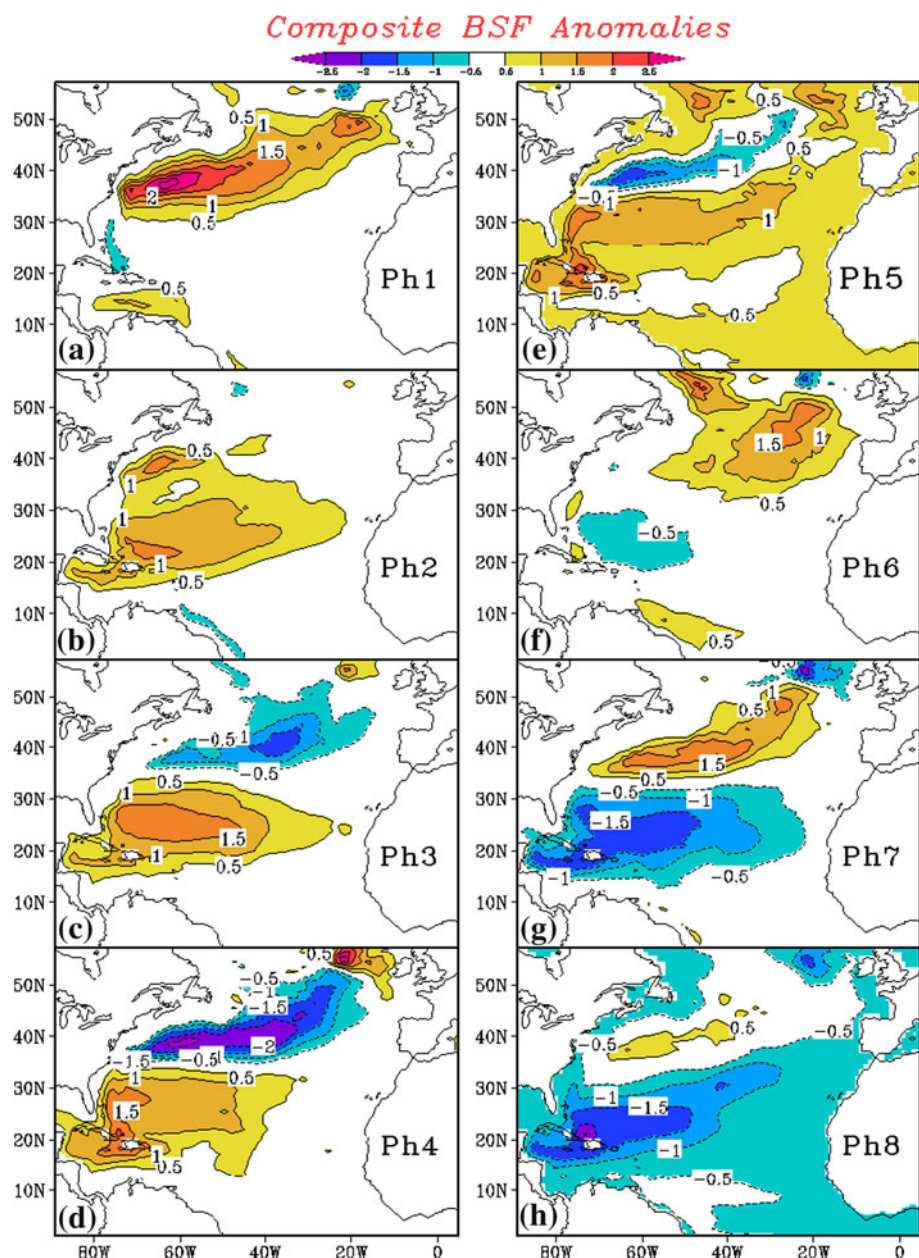
(Fig. 7b–d). When the delayed subtropical negative feedback becomes dominant, the anomalous negative deep overturning starts to weaken (Fig. 7c–d). The other half of the lifecycle is a mirror image of the above processes with the negative tropical HCA (Fig. 9f–h) paired with the negative STCA (Fig. 7f–h). This suggests that the STCA is a part of the wind-driven process in the subtropical and tropical Atlantic.

The wind-driven STCA modulates the meridional heat transport into the mid-latitude North Atlantic, which changes the HCA and SSTA in the mid-latitudes and hence weakens the positive feedback there. This contribution can be estimated by comparing the total anomalous heat transport (Fig. 10a) with those by the currents in the upper 460 m (Fig. 10b). The strong anomalous northward heat transport within 10°S–10°N in Phase 2 (Fig. 10a, b) is apparently due to the positive STCA during this period (Fig. 7b). Accompanying the persistence of positive STCA, the northward transport in the tropics continues until Phase 5 in the upper ocean (Fig. 10b). In Phase 4, the northward heat transport as high as 20 terawatts (10^{12} Watts) extending from the equator to about 30°N is mainly because the STCA is elongated to the mid-latitude (Fig. 7d). Therefore, even though the climatological STC is largely confined within the subtropics, the northward expansion of the STCA can be an important effect into the mid-latitudes. Compared with Phase 2, the negative transport in the upper ocean in Phases 7–8 is weaker because the negative STCAs are weaker than the positive ones. However, the pattern is still consistent.

The wind-driven gyre circulation accompanying the STCAs can also be seen from the oceanic barotropic stream function anomalies (BSFA, Fig. 15). In general, an anomalous anticyclonic gyre is developed between 20°N and 40°N during Phases 2–4 (Fig. 15b–d) while a cyclonic one is in Phases 6–8 (Fig. 15f–h). This oceanic response is consistent with the subtropical wind stress forcing described above. Further to the north, a narrower gyre is developed, opposite to the southern one. This BSFA pattern, especially its southern lobe, bears some resemblance to the anomalous ‘intergyre’ gyre, described by Marshall et al. (2001) and Czaja and Marshall (2001) as a slow oceanic response to the SLP changes, and affects the northward heat transport from the tropics. Specifically, the heat transport plays the role of eroding the SSTA and HCA in the western mid-latitude Atlantic. In fact, the BSFA at 25°N and AMOC transport at 35°N has a nearly out-of-phase relationship similar to the one between the deep and shallow overturning (not shown).

Furthermore, the averaged current anomalies for the upper 460 m in the western North Atlantic shows that northward anomalous western boundary current (AWBC) is initiated to the south of 25°N in Phase 2 (Fig. 16b), just

Fig. 15 The composite anomalies of the barotropic stream function in the eight phases of the lifecycle of the multidecadal AMOC oscillation as shown in Fig. 7 for **a** Phase 1, **b** Phase 2, **c** Phase 3, **d** Phase 4, **e** Phase 5, **f** Phase 6, **g** Phase 7 and **h** Phase 8. The contour interval is 0.5 Sv with the zero lines omitted. The color bar for the shading is shown at the top

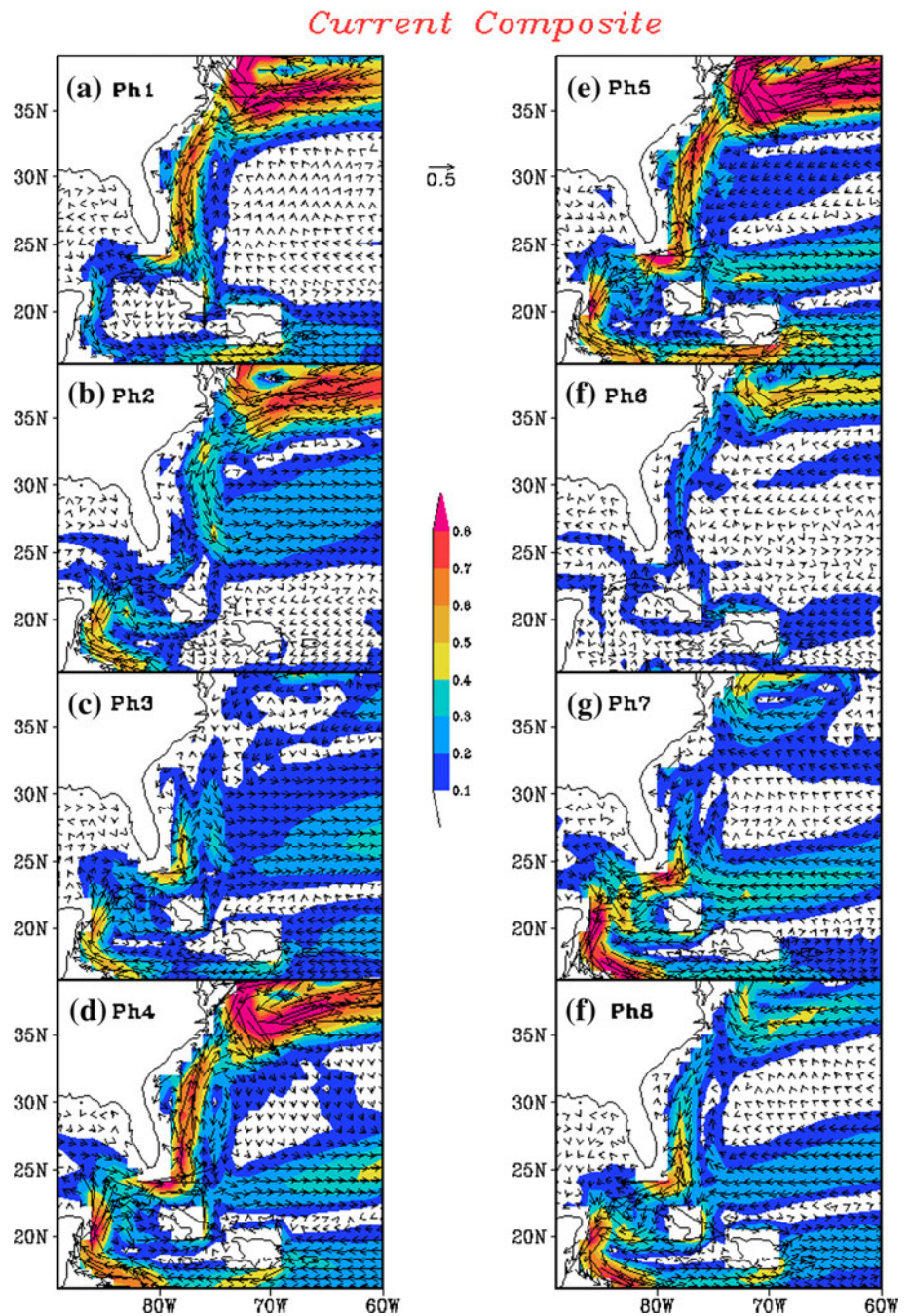


as the positive STCA starts (Fig. 7b) and the warm HCA forms near the western coast in the tropics (Fig. 9b). The AWBC counters the southward extension of the southwestward flow along the western coast from 35°N, which is associated with cold HCA extending from 40°N (Fig. 9b). In the next three phases, the northward AWBC strengthens and expands further north (Fig. 16c–e). This is associated with the enhancement of the warm HCA in the western tropical Atlantic (Fig. 9c) and its expansion produces a wedge of the warm HCA in the western ocean between 30°N and 40°N (Fig. 9d–e). The HCA is associated with the SSTA in the western Atlantic between 30°N and 40°N first appearing in Phase 4 (Fig. 8d) and substantially enhanced in Phase 5 (Fig. 8e). As we have pointed out

before, the transition from the cold to the warm phase (or vice versa) starts from the SSTA and HCA in the western Atlantic between 30°N and 40°N in Phase 4.

In summary, the quasi 30-year oscillation of the AMOC is associated with a positive air–sea feedback between the deep overturning and the SST-induced surface wind anomalies in the mid-latitude North Atlantic and a negative feedback between the STCA and the mid-latitude deep overturning. The subtropical–extratropical interaction involves both thermodynamic air–sea interaction and oceanic dynamics: The WES feedback plays a crucial role in expanding the AMOC-induced mid-latitude SST and wind anomalies into the subtropical ocean while the wind stress anomalies over the tropical Atlantic Ocean drive the

Fig. 16 The composite anomalies of the mean current averaged for the upper 460 m in the eight phases of the lifecycle of the multidecadal AMOC oscillation as shown in Fig. 7 for **a** Phase 1, **b** Phase 2, **c** Phase 3, **d** Phase 4, **e** Phase 5, **f** Phase 6, **g** Phase 7 and **h** Phase 8. The vector in the *upper center* represents current magnitude of 0.5 cm s^{-1} . The current magnitude is also shown by the *shading* on the maps. The *color bar* for the shading is shown at the center (unit: cm s^{-1})



anomalous gyre and STCA. A schematic diagram of the major feedback loops is presented in Fig. 17.

The proposed mechanism may provide new insight into several aspects of the AMOC variability. For instance, it explains why there is a nearly out-of-phase relationship between the STCA and the AMOC fluctuation in the CFS. Some previous studies (Jochum and Malanotte-Rizzoli 2001; Chang et al. 2008; Wen et al. 2010) have found that the STC strengthens when the AMOC weakens. However, these previous studies suggest that the STC strengthening

mainly is a result of less cancellation from the AMOC upper branch. Our results suggest that a portion of the STCA is a response to the AMOC-induced surface wind changes in the subtropics, which may play an active role during the oscillation. This mechanism also explains why the SSTA and HCA have opposite signs in the tropical Atlantic. The HCA is wind driven related to Ekman pumping, while SSTA is fluxes driven related to latent heat flux. This out-of-phase relationship between the SSTA and HCA has been found as a signature of the AMOC

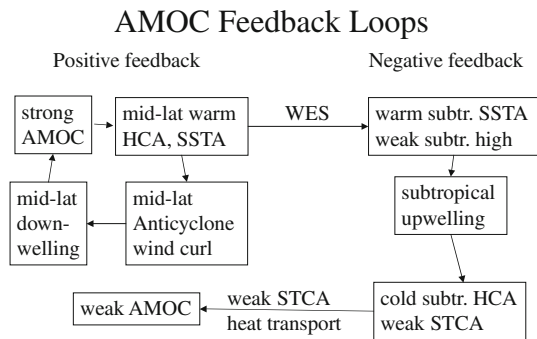


Fig. 17 Schematic diagram of the feedback loops for the AMOC oscillation. The closed loop in the left-hand side denotes the steps of the positive feedback in the mid-latitudes. The right-hand side shows the steps of the negative feedback from the subtropical Atlantic to the mid-latitude ocean. The direction of the evolution is pointed by the arrows

multidecadal variability by Zhang (2007) in a climate model simulation and in observations but has not been fully understood, as far as we know.

6 Summary and discussion

In this paper, we have analyzed the mean state and variability of the AMOC from a 335-year simulation of the CFS. It is found that the CFS produces a realistic pattern of the AMOC circulation with mean transport and seasonal cycle consistent with observation-based estimates. On multidecadal time scales, the AMOC variability is dominated by an intermittent quasi oscillation with 30-year period, based on the independent analyses of two statistical methods, the multichannel singular spectrum analysis (MSSA) and the EEMD. A phase composite procedure based on the MSSA modes is used to construct the lifecycle of the oscillation and analyze its mechanisms.

It is found that the AMOC oscillation is associated with the evolution of an anomalous deep overturning cell between 30°N and 50°N, which extends to the tropical ocean at levels below 500 m. This mid-latitude deep overturning is associated with the fluctuation of an oppositely rotating STCA with a phase lag of several years. Due to the enhanced northward heat transport by the positive deep overturning, warm HCA and SSTA are formed in 30°N–50°N across the Atlantic. The anomalous meridional SST gradient generates anticyclonic wind anomalies in mid-latitudes, which cause downwelling and enhance the overturning cell. Furthermore, the easterly wind anomalies between 30°N and 40°N also initiate the WES feedback to expand the warm mid-latitude SSTA into the tropical Atlantic Ocean and form a basin-wide horseshoe-shaped SSTA pattern. This process weakens the subtropical high and the trade winds. The resulting subtropical cyclonic

wind anomalies force the shoaling of the thermocline and generate cold HCA. This process weakens the subtropical gyre and induces negative STCA, which reduces the northward upper ocean transport and erodes the mid-latitude SSTA and HCA by weakening the western boundary current. As a result, the mid-latitude deep cell is weakened, mostly due to the reversal of the HCA and SSTA anomalies first appearing in the western Atlantic around 30°N–40°N.

The fluctuations in the northern hemisphere have ramifications in the southern hemisphere through the displacement of the ITCZ and its effects on the southeast trade winds, as well as the STCA, supposedly due to the associated Ekman pumping. In fact, there are some indications that the WES feedback originating from the northern mid-latitude ocean extends across the equator in the CFS. For instance, the warm SSTAs in the northern tropical Atlantic can shift the ITCZ northward, which enhances the southeast trade winds and causes cold contemporary SSTA in the southern tropical Atlantic (Fig. 8g–h), as already described by Zhang and Delworth (2005).

Although we have shown that the positive and negative feedbacks are active in the quasi 30-year oscillation, further evidence is needed to confirm that they are the cause of the oscillation. The relative strengths of the feedbacks need to be quantified to demonstrate the couplings are strong enough to generate an oscillation. The timescale of the oscillation also need to be accounted for, especially on how it relates to the hypothesized mechanism. For the first question, our results suggest that the deep overturning anomalies and the STCA have comparable magnitudes (Fig. 7) and provide similar amounts of meridional heat transports (30–40 terawatts in their peaks), which implies that the strength of the delayed negative feedback from the tropics is comparable to the positive one in the mid-latitudes. However, more definitive demonstration of their respective roles requires further sensitivity experiments to disconnect some of the links in the chain of feedback loops shown in Fig. 17 and thus eliminate one of the feedbacks. One possible way is to disconnect the air-sea coupling in momentum and heat flux separately, which eliminates either the Ekman pumping or WES feedback, two key processes in our scenario, to see how they affect the oscillation respectively. This kind of sensitivity experiments will be the next step of this study.

For the second question, we propose that the time scale of the oscillation is determined jointly by the characteristic time scales of the mid-latitude and subtropical feedbacks. Ideally, one would develop a box model for the AMOC based on the proposed feedbacks (e.g., Marshall et al. 2001; Ou 2011) and show that, with reasonable parameters, oscillations on the ~30 year timescale can be generated. In practice, however, an accurate estimate of these parameters can be difficult and such a theoretical study is

beyond the scope of this study. On the other hand, based on results from previous studies, it seems reasonable to expect oscillations at the required timescale. Recent studies have suggested that the AMOC has 20 to 30-year variability at mid-latitude band in both observations and models (e.g., Frankcombe and Dijkstra 2009; Frankcombe et al. 2010). In particular, theoretical studies show that temperature anomalies propagate westward as large-scale oceanic waves on this time scale (e.g., Huck et al. 1999). Recently, Sévellec and Fedorov (2011) found a weakly damped eigenmode of 24-year in an uncoupled ocean model associated with westward propagating temperature anomalies between 30°N and 60°N in the North Atlantic. In the CFS, the center of the SLPA tends to be established near the mid-latitude eastern Atlantic. The corresponding upwelling/downwelling anomaly generates the HCA that then extend southwestward in 30°N–50°N (Fig. 9), roughly resembling these theoretical results. It implies that the atmospheric wind anomalies are in a favorable position to stimulate the Rossby waves. We understand that these previous works deal with ocean internal modes. How air-sea coupling affects these modes should be further studied.

The processes governing the STCA evolution in the CFS are essentially similar to the ‘intergyre’ gyre by Marshall et al. (2001), even though they do not deal directly with the wind stress induced by the mid-latitude AMOC forcing. The preferred time scale in these previous studies is decadal, which is the intrinsic time scale of the subtropical fluctuation. The more persistent wind anomalies in the subtropical ocean induced from the mid-latitude may prolong the STCA and make it feedback to the slower mid-latitude process. Our results suggest that a crucial effect of the subtropical processes is on the subsurface temperatures around 30°N–40°N near the western boundary, which has attracted attention previously. We speculate that this interference between the tropical and extratropical processes also affects the time scale of the oscillation in the CFS.

Other aspects of the hypothetical mechanism also need further examination. Partly due to the restriction of the model configuration, this AMOC oscillation is mainly associated with surface and subsurface temperature anomalies. Therefore, the mechanism we have outlined above is different from those in several other models (e.g., Delworth et al. 1993; Danabasoglu 2008), where the salinity plays a more active role. As we have described above, thermal driven overturning also appears in other coupled systems (e.g., Zhu and Jungclaus 2008) although their mechanistic explanations may be different from ours.

Overall, the 30-year oscillation in the CFS is mainly wind-driven. This overturning anomaly occurs near a band of up to about 1 Sv Ekman transport near 30°N and has a form reminiscent of the overturning anomalies driven by

high latitude wind stress anomalies (Klinger and Cruz 2009; see their Fig. 3). The strongest full-column overturning anomaly tends to be more confined in latitudes (Fig. 7b, e, f) than one would expect from an AMOC variation driven by high-latitude density anomalies. Including thermohaline processes, Dong and Sutton (2005; see their Fig. 3b) show a less confined stream function anomaly.

The WES mechanism that links the extratropical and tropical surface anomalies in the CFS seems also different from the Johnson and Marshall’s (2002) equatorial buffer mechanism about the AMOC-induced tropical response, which suggests that the equator prevents coastal Kelvin waves induced by AMOC anomalies from entering the southern hemisphere, which causes an anomalous heat divergence in the northern tropical Atlantic with a corresponding SST change. This oceanic process seems to require longer delay between the high latitude and tropical SSTAs than that generated in the CFS 30-year oscillation. In this aspect, our results are more in line with the results of the water-hosing experiments and also consistent with the analysis of Zhang (2007). Moreover, the rough resemblance between the horseshoe-shaped SSTA pattern in certain phases of the oscillation and the observed AMO suggests that the AMOC-provoked WES feedback is a major climate influence of the AMOC multidecadal variability.

Finally, it is not clear as to what extent the mid-latitude overturning anomalies can contribute to the total AMOC fluctuation and interact with the thermohaline circulation driven by surface density anomalies, as discussed by Delworth et al. (1993) and others, and to what extent this interaction can affect the upper ocean circulation in the tropical and subtropical Atlantic. More recently, by analyzing the AMOC variations in the GODAS ocean analysis, Huang et al. (2011b) found that the AMOC seemed to have experienced nearly a full cycle during the past 30 years. They suggested that the AMOC is largely driven by the momentum and heat fluxes related to NAO, and temperature anomalies play dominant role. Further study is needed to demonstrate the role of the tropical ocean in the multi-decadal variations of the Atlantic Ocean using more sophisticated models and observational data.

Acknowledgments The authors would like to thank Drs. J. Shukla, J. Kinter and A. Kumar for their support and guidance of this project. We thank two anonymous reviewers for their constructive comments and suggestions. We also thank Drs. Boyin Huang, Shaoqing Zhang, Sirpa Häkkinen, Young-Gyu Park and Caihong Wen for beneficiary discussions and useful suggestions. We are grateful to Drs. C. Stan and V. Krishnamurthy for reviewing and editing an early version of the manuscript carefully and for making many constructive suggestions. Bohua Huang is supported by the NOAA CVP Program (NA07OAR4310310). Zhaohua Wu is supported by the National Science Foundation project AGS-1139479. The CFS simulation was carried out on the NCAR supercomputing system.

References

- Alvarez-Garcia F, Latif M, Biastoch A (2008) On multidecadal and quasi-decadal North Atlantic variability. *J Clim* 21:3433–3452
- Balmaseda MA, Smith GC, Haines K, Anderson D, Palmer TN, Vidard A (2007) Historical reconstruction of the Atlantic Meridional overturning circulation from the ECMWF operational ocean reanalysis. *Geophys Res Lett* 34:L23615. doi:[10.1029/2007GL031645](https://doi.org/10.1029/2007GL031645)
- Behringer DW, Xue Y (2004) Evaluation of the global ocean data assimilation system at NCEP: the Pacific Ocean. In: Eighth symposium on integrated observing and assimilation systems for atmosphere, oceans, and land surface, AMS 84th annual meeting, Washington State Convention and Trade Center, Seattle, Washington, 11–15
- Böning CW, Scheinert M, Dengg J, Biastoch A, Funk A (2006) Decadal variability of subpolar gyre transport and its reverberation in the North Atlantic overturning. *Geophys Res Lett* 33:L21S01. doi:[10.1029/2006GL026906](https://doi.org/10.1029/2006GL026906)
- Broccoli AJ, Dahl KA, Stouffer RJ (2006) Response of the ITCZ to Northern Hemisphere cooling. *Geophys Res Lett* 33:L01702. doi:[10.1029/2005GL024546](https://doi.org/10.1029/2005GL024546)
- Chang P, et al (2008) Oceanic link between abrupt changes in the North Atlantic Ocean and the African monsoon. *Nat Geosci* 1:444–448
- Chang P, Ji L, Li H (1997) A decadal climate variation in the tropical Atlantic Ocean from thermodynamic air–sea interactions. *Nature* 385:516–518
- Cheng W, Bleck R, Rooth C (2004) Multi-decadal thermohaline variability in an ocean–atmosphere general circulation model. *Clim Dyn* 22:573–590
- Chiang JCH, Bitz CM (2005) Influence of high latitude ice cover on the marine intertropical convergence zone. *Clim Dyn* 25:477–496
- Chiang JCH, Cheng W, Bitz CM (2008) Fast teleconnections to the tropical Atlantic sector from Atlantic thermohaline adjustment. *Geophys Res Lett* 35:L07704. doi:[10.1029/2008GL033292](https://doi.org/10.1029/2008GL033292)
- Czaja A, Marshall J (2001) Observations of atmosphere–ocean coupling in the North Atlantic. *Q J R Meteorol Soc* 127:1893–1916
- Dahl KA, Broccoli AJ, Stouffer RJ (2005) Assessing the role of North Atlantic freshwater forcing in millennial scale climate variability: a tropical Atlantic perspective. *Clim Dyn* 24:325–346
- Danabasoglu G (2008) On multidecadal variability of the Atlantic meridional overturning circulation in the community climate system model version 3. *J Clim* 21:5524–5544
- Delworth TL, Greatbatch RJ (2000) Multidecadal thermohaline circulation variability driven by atmospheric surface flux forcing. *J Clim* 13:1481–1495
- Delworth TL, Mann ME (2000) Observed and simulated multidecadal variability in the Northern Hemisphere. *Clim Dyn* 16:661–676
- Delworth TL, Manabe S, Stouffer RJ (1993) Interdecadal variations of the thermohaline circulation in a coupled ocean–atmosphere model. *J Clim* 6:1993–2011
- Delworth TL, Zhang R, Mann ME (2007) Decadal to centennial variability of the Atlantic from observations and models. In: Schmittner A, Chiang J, Hemmings S (eds) *Ocean circulation: mechanisms and impacts*. *Geophy Monogr Ser*, vol 173, pp 131–148
- Dong BW, Sutton RT (2002) Adjustment of the coupled ocean–atmosphere system to a sudden change in the thermohaline circulation. *Geophys Res Lett* 29:1728. doi:[10.1029/2002GL015229](https://doi.org/10.1029/2002GL015229)
- Dong BW, Sutton RT (2005) Mechanism of interdecadal thermohaline circulation variability in a coupled ocean–atmosphere GCM. *J Clim* 18:1117–1135
- Eden C, Willebrand J (2000) Mechanism of interannual to decadal variability of the North Atlantic circulation. *J Clim* 14:2266–2280
- Enfield DB, Mestas-Nunez AM PJ, Trimble PJ (2001) The Atlantic multidecadal oscillation and its relation to rainfall and river flows in the continental U.S. *Geophys Res Lett* 28:2077–2080
- Folland CK, Palmer TN, Parker DE (1986) Sahel rainfall and worldwide sea temperatures. *Nature* 320:602–607
- Frankcombe LM, Dijkstra HA (2009) Coherent multidecadal variability in North Atlantic sea level. *Geophys Res Lett* 36:L15 604. doi:[10.1029/2009GL039455](https://doi.org/10.1029/2009GL039455)
- Frankcombe LM, von der Heydt A, Dijkstra HA (2010) North Atlantic multidecadal climate variability: an investigation of dominant time scales and processes. *J Clim* 23:3626–3638
- Ganachaud A, Wunsch C (2000) Improved estimates of global ocean circulation, heat transport and mixing from hydrographic data. *Nature* 408:453–457
- Gent PR, McWilliams JC (1990) Isopycnal mixing in ocean circulation models. *J Phys Oceanogr* 20:150–155
- Ghil M, Allen MR, Dettinger MD, Ide K, Kondrashov D, Mann ME, Robertson AW, Saunders A, Tian Y, Varadi F, Yiou P (2002) Advanced spectral methods for climatic time series. *Rev Geophys* 40:1003. doi:[10.1029/2000RG000092](https://doi.org/10.1029/2000RG000092)
- Gray ST, Graumlich LJ, Betancourt JL, Pedersen GT (2004) A tree-ring based reconstruction of the Atlantic multidecadal oscillation since 1567 A.D. *Geophys Res Lett* 31:L12205. doi:[10.1029/2004GL019932](https://doi.org/10.1029/2004GL019932)
- Häkkinen S, Rhines PB (2009) Shifting surface currents in the northern North Atlantic Ocean. *J Geophys Res* 114:C04005. doi:[10.1029/2008JC004883](https://doi.org/10.1029/2008JC004883)
- Hu Z–Z, Nitta T (1996) Wavelet analysis of summer rainfall over North China and India and SOI using 1891–1992 data. *J Meteorol Soc Jpn* 74:833–844
- Hu A, Otto-Bliessner BL, Meehl GA, Han W, Morrill C, Brady EC, Briegleb B (2008) Response of thermohaline circulation to freshwater forcing under present day and LGM conditions. *J Clim* 21:2239–2258
- Hu Z–Z, Huang B, Kinter III JL, Wu Z, Kumar A (2011) Connection of stratospheric QBO with global atmospheric general circulation and tropical SST. Part II: interdecadal variations. *Clim Dyn*. doi:[10.1007/s00382-011-1073-6](https://doi.org/10.1007/s00382-011-1073-6) (published online)
- Huang NE, et al (1998) The empirical mode decomposition and the Hilbert spectrum for nonlinear and non-stationary time series analysis. *Proc R Soc Lond A* 454:903–993
- Huang NE, Wu Z (2008) A review on Hilbert–Huang transform: the method and its applications on geophysical studies. *Rev Geophys* 46:RG2006. doi:[10.1029/2007RG000228](https://doi.org/10.1029/2007RG000228)
- Huang B, Hu Z–Z, Kinter III JL, Wu Z, Kumar A (2011a) Connection of stratospheric QBO with global atmospheric general circulation and tropical SST. Part I: methodology and composite life cycle. *Clim Dyn*. doi:[10.1007/s00382-011-1250-7](https://doi.org/10.1007/s00382-011-1250-7)
- Huang B, Xue Y, Kumar A, Behringer DW (2011b) AMOC variations in 1979–2008 simulated by NCEP operational ocean data assimilation system. *Clim Dyn* (in press)
- Huck T, Colin de Verdière A, Weaver AJ (1999) Interdecadal variability of the thermohaline circulation in box-ocean models forced by fixed surface fluxes. *J Phys Oceanogr* 29:865–892
- Huck T, Vallis GK, Colin de Verdière A (2001) On the robustness of the interdecadal modes of the thermohaline circulation. *J Clim* 14:940–963
- Jochum M, Malanotte-Rizzoli P (2001) Influence of the meridional overturning circulation on tropical–subtropical pathways. *J Phys Oceanogr* 31:1313–1323
- Johns WE, Baringer MO, Beal LM, Cunningham SA, Kanzow T, Bryden HL, Hirschi JJM, Marotzke J, Meinen CS, Shaw B,

- Curry R (2011) Continuous, array-based estimates of Atlantic Ocean heat transport at 26.5°N. *J Clim* 24:2429–2449
- Johnson H, Marshall DP (2002) A theory for the surface Atlantic response to thermohaline variability. *J Phys Oceanogr* 32:1121–1132
- Jungclauss JH, Haak H, Latif M, Mikolajewicz U (2005) Arctic–North Atlantic interactions and multidecadal variability of the meridional overturning circulation. *J Clim* 18:4013–4031
- Kanamitsu M, Ebisuzaki W, Woollen J, Yang S-K, Hnilo JJ, Fiorino M, Potter GL (2002) NCEP–DOE AMIP-II reanalysis (R-2). *Bull Am Meteorol Soc* 83:1631–1643
- Kerr RA (2000) A North Atlantic climate pacemaker for the centuries. *Science* 288:1984–1985
- Klinger B, Cruz C (2009) Decadal response of global circulation to Southern Ocean zonal wind stress perturbation. *J Phys Oceanogr* 39:1888–1904
- Knight JT, Allan RJ, Folland CK, Vellinga M, Mann ME (2005) A signature of persistent natural thermohaline circulation cycles in observed climate. *Geophys Res Lett* 32:L20708. doi:10.1029/2005GL024233
- Kushnir Y (1994) Interdecadal variations in North Atlantic Sea surface temperature and associated atmospheric conditions. *J Clim* 7:142–157
- Large WG, McWilliams JC, Doney SC (1994) Oceanic vertical mixing: a review and a model with a nonlocal boundary layer parameterization. *Rev Geophys* 32:363–403
- Latif M, Collins M, Pohlmann H, Keenlyside N (2006) A review of predictability studies of the Atlantic sector climate on decadal time scales. *J Clim* 19:5971–5987
- Lindzen RS, Nigam S (1987) On the role of sea surface temperature gradients in forcing low-level winds and convergence in the tropics. *J Atmos Sci* 44:2418–2436
- Liu Z (1994) A simple model of the mass exchange between the subtropical and tropical ocean. *J Phys Oceanogr* 24:1153–1165
- Lumpkin R, Speer K (2003) Large-scale vertical and horizontal circulation in the North Atlantic Ocean. *J Phys Oceanogr* 33:1902–1920
- Lumpkin R, Speer K (2007) Global ocean meridional overturning. *J Phys Oceanogr* 37:2550–2562
- Mahajan S, Saravanan R, Chang P (2010) Free and forced variability of the tropical Atlantic Ocean: role of the wind–evaporation–sea surface temperature feedback. *J Clim* 23:5958–5977
- Manabe S, Stouffer RJ (1988) Two stable equilibria of a coupled ocean–atmosphere model. *J Clim* 1:841–866
- Marshall J, Johnson H, Goodman J (2001) A study of the interaction of the North Atlantic Oscillation with the ocean circulation. *J Clim* 14:1399–1421
- McCreary JP, Lu P (1994) Interaction between the subtropical and equatorial ocean circulations: the subtropical cell. *J Phys Oceanogr* 24:466–497
- Moron V, Vautard R, Ghil M (1998) Trends, interdecadal and interannual oscillations in global sea-surface temperatures. *Clim Dyn* 14:545–569
- Ou H-S (2011) A minimal model of the Atlantic multidecadal variability: its genesis and predictability. *Clim Dyn*. doi:10.1007/s00382-011-1007-3 (published online)
- Pacanowski RC, Griffies SM (1998) MOM 3.0 manual. NOAA/GFDL http://www.gfdl.noaa.gov/~smg/MOM/web/guide_parent/guide_parent.html
- Park Y-G, Hwang JH (2009) Local advective mechanism for interdecadal variability in circulations driven by constant surface heat fluxes in idealized basins. *J Oceanogr* 65:549–566
- Plaut G, Vautard R (1994) Spells of low-frequency oscillations and weather regimes in the Northern Hemisphere. *J Atmos Sci* 51:210–236
- Saha S, et al (2006) The NCEP climate forecast system. *J Clim* 19:3483–3517
- Schopf PS, Suarez MJ (1988) Vacillations in a coupled ocean–atmosphere model. *J Atmos Sci* 45:549–566
- Schott FA, McCreary JP, Johnson GC (2004) Shallow overturning circulations of the tropical–subtropical oceans, in earth climate: the ocean–atmosphere interaction, AGU, pp 261–304
- Semenov VA, Latif M, Dommenget D, Keenlyside NS, Strehz A, Martin T, Park W (2010) The impact of North Atlantic–Arctic multidecadal variability on northern hemisphere surface air temperature. *J Clim* 23:5668–5677
- Sévellec F, Fedorov AV (2011) An interdecadal oscillatory eigenmode of the Atlantic meridional overturning circulation in a realistic ocean GCM. *J Clim*, submitted
- Sime LC, Stevens DP, Heywood KJ, Oliver KIC (2006) A decomposition of the Atlantic meridional overturning. *J Phys Oceanogr* 36:2253–2270
- Stouffer RJ, et al (2006) Investigating the causes of the response of the thermohaline circulation to past and future climate changes. *J Clim* 19:1365–1387
- Suarez MJ, Schopf PS (1988) A delayed action oscillator for ENSO. *J Atmos Sci* 45:3283–3287
- Sutton RW, Hodson DLR (2007) Climate response to basin-scale warming and cooling of the North Atlantic Ocean. *J Clim* 20:891–907
- Talley LD, Reid JL, Robbins PE (2003) Data-based meridional overturning stream function for the global ocean. *J Clim* 16:3213–3226
- Te Raa L, Dijkstra HD (2002) Instability of the thermohaline ocean circulation on interdecadal timescales. *J Phys Oceanogr* 32:138–160
- Timmermann A, Latif M, Voss R, Grötzner A (1998) Northern hemispheric interdecadal variability: a coupled air–sea mode. *J Clim* 12:2607–2624
- Timmermann A, An S, Krebs U, Goosse H (2005) ENSO suppression due to a weakening of the North Atlantic thermohaline circulation. *J Clim* 18:3122–3139
- Ting M, Kushnir Y, Seager R, Li C (2010) Atlantic multidecadal variability and its climate impacts in CMIP3 models and observations. In: 2010 US AMOC annual meeting, Miami, FL. <http://www.atlanticmoc.org/AMOC2010agenda.php>
- Vellinga M, Wood R (2002) Global climatic impacts of a collapse of the Atlantic thermohaline circulation. *Clim Change* 54:251–267
- Vellinga M, Wu P (2004) Low-latitude freshwater influences on centennial variability of the Atlantic thermohaline circulation. *J Clim* 17:4498–4511
- Weaver AJ, Sarachik ES (1991) Evidence for decadal variability in an ocean general circulation model: an advective mechanism. *Atmos–Ocean* 29:197–231
- Weaver AJ, Valcke S (1998) On the variability of the thermohaline circulation in the GFDL coupled model. *J Clim* 11:759–767
- Wen C, Chang P, Saravanan R (2010) Effect of the Atlantic overturning circulation changes on the tropical Atlantic sea-surface temperature variability: a 2–1/2 layer reduced gravity ocean model study. *J Clim* 23:312–332
- Weng W, Neelin JD (1998) On the role of ocean–atmosphere interaction in midlatitude interdecadal variability. *Geophys Res Lett* 25:167–170
- Wu Z, Huang NE (2009) Ensemble empirical mode decomposition: a noise-assisted data analysis method. *Adv Adapt Data Anal* 1:1–41
- Wu Z, Huang NE, Wallace JM, Smoliak BV, Chen X (2011) On the time-varying trend in global-mean surface temperature. *Clim Dyn* (revised)
- Xie S-P (1999) A dynamic ocean–atmosphere model of the tropical Atlantic decadal variability. *J Clim* 12:64–70
- Zhang R (2007) Anticorrelated multidecadal variations between surface and subsurface tropical North Atlantic. *Geophys Res Lett* 34:L12713. doi:10.1029/2007GL030225

Zhang R, Delworth TL (2005) Simulated tropical response to a substantial weakening of the Atlantic thermohaline circulation. *J Clim* 18:1853–1860

Zhu X, Jungclaus J (2008) Interdecadal variability of the meridional overturning circulation as an ocean internal mode. *Clim Dyn* 31:731–741. doi:[10.1007/s00382-008-0383-9](https://doi.org/10.1007/s00382-008-0383-9)